



1

2 **Title:** Quantification of Drought During the Collapse of the Classic Maya  
3 Civilization

4

5 **Authors:** Nicholas P. Evans<sup>1\*</sup>, Thomas K. Bauska<sup>1</sup>, Fernando Gázquez<sup>1</sup>, Mark  
6 Brenner<sup>2</sup>, Jason H. Curtis<sup>2</sup>, and David A. Hodell<sup>1</sup>

7 **Affiliations:**

8 <sup>1</sup>Godwin Laboratory for Palaeoclimate Research, Department of Earth Sciences,  
9 University of Cambridge, Downing Street, Cambridge, CB2 3EQ, United Kingdom.

10 <sup>2</sup>Department of Geological Sciences, University of Florida, Gainesville, FL 32611,  
11 USA.

12 \*Correspondence to: ne243@cam.ac.uk.

13 **Abstract:**

14

15 The demise of Lowland Classic Maya civilization during the Terminal Classic Period  
16 (~800-1000 C.E.) is a well-cited example of how past climate may have impacted  
17 ancient societies. Attempts to estimate the magnitude of hydrologic change, however,  
18 have met with equivocal success because of the qualitative and indirect nature of  
19 available climate proxy data. We reconstructed the past isotopic composition ( $\delta^{18}\text{O}$ ,  
20  $\delta\text{D}$ ,  $^{17}\text{O}$ -excess and d-excess) of water in Lake Chichancanab, Mexico, using a novel  
21 technique that involves isotopic analysis of the structurally bound water in  
22 sedimentary gypsum, which was deposited under drought conditions. The triple  
23 oxygen and hydrogen isotope data provide a direct measure of past changes in lake  
24 hydrology. We modeled the data and conclude that annual precipitation decreased  
25 between 41 and 54%, with intervals of up to 70% rainfall reduction during peak  
26 drought conditions, and relative humidity declined by 2 to 7% compared to today.

27

28 **One Sentence Summary:**

29

30 We present quantitative estimates of hydro-climate changes that coincided with the  
31 demise of the Classic Maya civilization.

32

33 **Main Text:**

34

35 More than two decades ago, a sediment core from Lake Chichancanab  
36 (Yucatán Peninsula, Mexico; Fig. S1) provided the first physical evidence of a  
37 temporal correlation between drought and the sociopolitical transformation of the  
38 Classic Maya civilization during the Terminal Classic Period (TCP) (1). Presence of  
39 gypsum horizons and a concomitant increase in the oxygen isotope ratio ( $^{18}\text{O}/^{16}\text{O}$ ) in  
40 shells of ostracods and gastropods suggested the TCP was among the driest periods of  
41 the Holocene in northern Yucatán. Paleoclimate records produced subsequently  
42 provided additional evidence for drought during the TCP (2-9), but the magnitude of  
43 hydro-climate change and its influence on Maya agricultural and sociopolitical  
44 systems remains controversial (10). The qualitative nature of most climate proxy

45 archives, combined with dating uncertainties, has prevented detailed assessment of  
46 the relationship between past climate and cultural changes (10-12).

47

48         Recent attempts to quantify estimates of past changes in rainfall amount and  
49 assess the impact on ancient Maya agriculture have utilized either oxygen ( $\delta^{18}\text{O}$ ) (6,  
50 13) or hydrogen ( $\delta\text{D}$ ) (9-11) isotopes. No study to date has combined the two isotope  
51 systems because materials used for analysis, e.g., carbonates and leaf waxes, preclude  
52 simultaneous measurement of the multiple isotopologues of water. Combined analysis  
53 of  $\delta^{18}\text{O}$ ,  $\delta^{17}\text{O}$  and  $\delta\text{D}$  is a powerful method to estimate past hydrologic changes  
54 quantitatively because hydrogen and triple oxygen isotopes each undergo slightly  
55 different fractionation during evaporation, leading to changes in the derived d-excess  
56 ( $\delta\text{D} - 8 \cdot \delta^{18}\text{O}$ ) and  $^{17}\text{O}$ -excess ( $\ln[\delta^{17}\text{O} + 1] - 0.528 \ln[\delta^{18}\text{O} + 1]$ ) parameters (14-19).  
57 In an effectively closed hydrological basin such as Lake Chichancanab, the primary  
58 controls on the isotopic fractionation of lake water during evaporation include: the  
59 fractional loss of precipitation to evaporation (P/E), normalized relative humidity  
60 ( $\text{RH}_n$ ), temperature, and changes in the precipitation source (1-3, 14). The d-excess is  
61 largely dependent on  $\text{RH}_n$  and temperature, whereas  $^{17}\text{O}$ -excess is controlled mainly  
62 by  $\text{RH}_n$  (14-19). Because the predicted trends of d-excess and  $^{17}\text{O}$ -excess in  
63 evaporating waters display different responses to climate variables, they can be  
64 evaluated individually using an iterative model (20).

65

66         We took advantage of the benefits of using all isotopologues of water and their  
67 derived parameters (d-excess and  $^{17}\text{O}$ -excess) by measuring triple oxygen and  
68 hydrogen isotopes in the hydration water of gypsum ( $\text{CaSO}_4 \cdot 2\text{H}_2\text{O}$ ) in sediment cores  
69 from Lake Chichancanab (Fig. S2) (3). Today, the lake water is near saturation for  
70 gypsum and during past periods of drier climate, when the lake volume shrank,  
71 gypsum precipitated from the lake water and was preserved as distinct layers within  
72 the accumulating sediments (1-3). When gypsum forms, water molecules are  
73 incorporated directly into its crystalline structure and this “gypsum hydration water”  
74 (GHW) records the isotopic composition of the parent fluid, with known isotopic  
75 fractionations (14, 17, 21-26). Unlike oxygen isotope fractionation during formation  
76 of carbonate minerals (27, 28), fractionation during gypsum crystallization is

77 practically independent of temperature (24), biological or kinetic (non-equilibrium)  
78 effects (17). Additionally, isotopes of GHW that are measured in the sedimented  
79 gypsum inherently record the driest periods, offering a distinct advantage over other  
80 traditional climate archives such as speleothems or mollusk shells, which may fail to  
81 register peak drought conditions because of growth hiatuses. Absolute differences in  
82 the  $\delta^{18}\text{O}$ ,  $\delta\text{D}$ ,  $^{17}\text{O}$ -excess and d-excess, between modern and paleo-lake water, provide  
83 an estimate of differences between the lake hydrologic budget during the TCP and  
84 today (Fig. 1). Results were evaluated using a numerical isotope mass balance model  
85 that must satisfy all isotope variables (20) (Fig. S3), and thus provides a more robust  
86 constraint on past hydrology than does modeling  $\delta^{18}\text{O}$  or  $\delta\text{D}$  alone.

87

88 The modern climate around Lake Chichancanab is characterized by a mean  
89 annual precipitation of  $\sim 1200$  mm, a mean annual surface water temperature of  $\sim 26^\circ\text{C}$   
90 and a net annual water deficit of 300-400 mm/yr (3, 22). Large changes in  
91 precipitation and  $\text{RH}_n$  occur between the dry (November to May) and rainy seasons  
92 (June to October) (13, 29). Measured  $\delta^{18}\text{O}$  and  $\delta\text{D}$  of precipitation and groundwater  
93 samples from the Yucatán Peninsula, collected from 1994 to 2010, define a local  
94 meteoric water line (LMWL) with slope 7.7 (Fig. 2). Evaporation enriches the lake in  
95 the heavier water isotopes ( $2.6\text{‰} < \delta^{18}\text{O} < 3.8\text{‰}$  and  $10.1\text{‰} < \delta\text{D} < 17.2\text{‰}$ ), evolving  
96 along an evaporative line defined by  $\delta\text{D} = 5.1 \cdot \delta^{18}\text{O} - 3.1$ . This evaporation line  
97 intersects the LMWL at  $\delta^{18}\text{O} = -4.7(\pm 1.2)\text{‰}$  and  $\delta\text{D} = -27.5(\pm 10.7)\text{‰}$ , which is  
98 within error of the mean oxygen and hydrogen isotope values recorded in local rivers  
99 and groundwater from regional IAEA GNIP stations ( $\delta^{18}\text{O} = -4.1\text{‰}$ ;  $\delta\text{D} = -24.3\text{‰}$ )  
100 (29) and this study ( $\delta^{18}\text{O} = -4.0\text{‰}$ ;  $\delta\text{D} = -23.5\text{‰}$ ).

101

102 The gypsum deposited during the droughts of the Terminal Classic and early  
103 Postclassic Periods was used to calculate the  $\delta^{18}\text{O}$ ,  $\delta^{17}\text{O}$  and  $\delta\text{D}$  of the paleo-lake  
104 water, which ranged from 3.6‰ to 4.9‰ for  $\delta^{18}\text{O}$ , 1.9‰ to 2.5‰ for  $\delta^{17}\text{O}$ , and  
105 13.7‰ to 18.8‰ for  $\delta\text{D}$  (Fig. 1). Mean values of the paleo-lake waters ( $\delta^{18}\text{O} = 4.2\text{‰}$ ;  
106  $\delta^{17}\text{O} = 2.2\text{‰}$ ;  $\delta\text{D} = 16.4\text{‰}$ ) during drought episodes are enriched in the heavier  
107 isotopes compared to modern lake values ( $\delta^{18}\text{O} = 3.1\text{‰}$ ;  $\delta^{17}\text{O} = 1.6\text{‰}$ ;  $\delta\text{D} = 12.7\text{‰}$ ).  
108 Age uncertainty associated with the lake record and periods of gypsum precipitation



109 was calculated using Bayesian age-depth analysis of radiocarbon ages obtained from  
110 the sediment cores (3) (Fig. 1). The probabilities of drought occurring specifically  
111 during the onset (~750 to ~850 C.E) and the end (~950 to ~1050 C.E.) of the TCP are  
112 high ( $P > 0.85$  and  $P > 0.95$ , respectively) (20). Multiple proxy climate records across  
113 the Maya Lowlands also provide evidence of drought synchronicity, with only slight  
114 temporal variations across the region (10).

115

116 To estimate quantitatively the magnitude of drought during the TCP, we  
117 employed a transient model that explicitly simulates the evolution of the isotopic and  
118 chemical composition of the lake water, including the gypsum flux to the lake  
119 sediments (Fig. S3). The modeled gypsum flux can be compared to observed  
120 variations in the gypsum content of the sediments, as expressed by variations in  
121 sediment bulk density (3). Changes in lake surface-area-to-volume ratio were  
122 obtained from the lake bathymetry (Fig. S4). The model was run at sub-monthly  
123 resolution in a series of millennial-duration experiments, forced with North American  
124 Regional Reanalysis (NARR) data for local precipitation and  $RH_n$ . We first tested the  
125 model using the climate forcing across the modern sampling period from 1994 to  
126 2010 (Fig. S5). It successfully reproduced the mean of modern isotope data, with  
127 insignificant gypsum precipitation. This time interval, which was fortuitously one of  
128 the driest of recent decades, was then used as the baseline for comparison to paleo-  
129 simulations.

130

131 To provide scenarios that are directly comparable to the GHW data, we  
132 performed long transient simulations in which rainfall and  $RH_n$  were reduced by  
133 variable amounts to simulate a series of multi-decadal-scale droughts. The use of a  
134 model allows us to compare, directly and quantitatively, climate conditions that affect  
135 the modern lake, with those of plausible drought conditions. First, only the intervals  
136 over which the model produced gypsum deposition (modeled sediment density  $>1.1$   
137  $\text{g/cm}^3$ ) were selected. The periods of modeled gypsum accumulation were then  
138 aggregated into drought conditions for a given scenario via two pathways: (i) all  
139 model variables were averaged across all of the droughts, and (ii) probability density  
140 functions were constructed incorporating the variability within and between each

141 decadal-length drought. Data consistent scenarios were then selected by excluding  
142 those model runs that fell outside the  $1\sigma$  range of the isotope data and where, on  
143 average, the model failed to produce significant gypsum accumulation (cutoff of  
144 average density  $<1.2 \text{ g/cm}^3$  based on  $1\sigma$  range; Fig. S6). Two possible scenarios were  
145 tested subsequently: (i) a reduction in precipitation with accompanying shifts in the  
146 isotopic composition of rainwater (i.e. the amount effect) and, (ii) a reduction in  
147 precipitation with accompanying decreases in  $\text{RH}_n$  (Fig. 3).

148

149 In the first scenario, precipitation  $\delta^{18}\text{O}$  was reduced with an increase in rainfall  
150 according to the amount effect relationship (i.e.,  $\delta^{18}\text{O}_{\text{precipitation}}/\Delta\text{Precipitation}_{\text{volume}} = -$   
151  $0.0121\text{‰}/\text{mm}$ ; Fig. S7) with associated changes in  $\delta\text{D}$  and  $\delta^{17}\text{O}$  that track the Global  
152 MWL (i.e., no changes in d-excess or  $^{17}\text{O}$ -excess). No scenarios with these  
153 assumptions are able to reproduce the relationship between  $\delta^{18}\text{O}$ , d-excess and  $^{17}\text{O}$ -  
154 excess observed in the data. If the constraints provided by d-excess and  $^{17}\text{O}$ -excess  
155 are removed and only  $\delta^{18}\text{O}$  and gypsum precipitation are employed, our model  
156 permits reductions in precipitation that average 50% over all drought intervals (Fig. 3,  
157 blue lines). This estimate is in broad agreement with previous work that relied on  
158 carbonate  $\delta^{18}\text{O}$ -derived precipitation estimates (using the local amount effect), which  
159 predicted reductions of up to 40% (6, 13). Our greater estimate of 50% is in part a  
160 consequence of the peak drought  $\delta^{18}\text{O}$  values recorded by gypsum, as well as the  
161 integration of simulated gypsum formation and true lake bathymetry in the model.  
162 Crucially, however, the added information from the d-excess and  $^{17}\text{O}$ -excess data  
163 suggests that multi-decadal shifts in the  $\delta^{18}\text{O}$  of precipitation (caused by the amount  
164 effect) were not the dominant factor that affected the isotope budget of Lake  
165 Chichancanab during the TCP.

166

167 In the second scenario, we reduced precipitation without changes in the  $\delta^{18}\text{O}$   
168 of precipitation, but instead with concurrent changes in  $\text{RH}_n$ . In this case we observed  
169 excellent agreement between the modeled evolution of all isotopic data, with  
170 increases in  $\delta^{18}\text{O}$  accompanied by decreases in d-excess and  $^{17}\text{O}$ -excess (Fig. 3, red  
171 lines). This analysis yielded plausible scenarios of precipitation reduction that average  
172 47% across all droughts (with a  $1\sigma$  level of 41-54%) accompanied by  $\text{RH}_n$  reductions

173 of 4% ( $1\sigma$  level 2-7%). This result provides a robust, quantitative estimate of the  
174 mean annual hydrological conditions of the combined drought periods during the TCP  
175 at Lake Chichancanab.

176

177 Although the time evolution of our model is not a direct reconstruction of  
178 climate conditions, the model permits heterogeneity within and between each decade-  
179 long drought. The  $\pm 1\sigma$  range determined from the probability density functions  
180 indicates that the precipitation reduction could vary from 20 to 70% throughout the  
181 modeled droughts (Fig. 3). This variability represents the transition into and out of  
182 drought phases and demonstrates that the severity of the droughts could be intense (up  
183 to a 70% reduction in precipitation), while maintaining the isotope balance and  
184 without desiccating the lake. Although variability in the seasonal delivery of rainfall  
185 (or lack thereof) is difficult to constrain because the residence time of the lake water  
186 is greater than an annual cycle, our results provide quantitative estimates for the total  
187 annual reduction in the water available for agriculture and domestic use for the  
188 ancient Maya. Importantly, recorded Colonial-period accounts of later droughts, e.g.,  
189 1535-1560 and 1765-1773, during which high mortality, famines, and population  
190 displacement were reported (30), are not manifest as intervals of gypsum precipitation  
191 in Lake Chichancanab. The lack of gypsum formation is likely a result of shorter  
192 duration and/or lower severity of these droughts, providing further evidence that the  
193 TCP was an unusually dry period for the Holocene on the Yucatán Peninsula.

194

195 Using triple oxygen and hydrogen isotope data to independently deconvolve  
196 climate variables precipitation,  $RH_n$  and the amount effect, we constrained the  
197 changing hydrological conditions at Lake Chichancanab. This approach provides a  
198 significant advance over previous attempts to estimate the magnitude of rainfall  
199 reduction during the TCP droughts (e.g. 6, 13). Furthermore, these quantitative  
200 estimates of past rainfall and  $RH_n$  can serve as input variables in crop models, to  
201 better understand how drought affected agriculture (e.g., maize production) in the  
202 northern Maya Lowlands during the TCP (12).

203 **References:**

204

205 [1] D. A. Hodell, J. H. Curtis, M. Brenner. Possible role of climate in the collapse of  
206 Classic Maya civilization. *Nature* **375** (6530), 391-394 (1995).

207

208 [2] D. A. Hodell, M. Brenner, J. H. Curtis, T. Guilderson. Solar forcing of drought  
209 frequency in the Maya lowlands. *Science* **292** (5520), 1367-1370 (2001).

210

211 [3] D. A. Hodell, M. Brenner, J. H. Curtis. Terminal Classic drought in the northern  
212 Maya lowlands inferred from multiple sediment cores in Lake Chichancanab  
213 (Mexico). *Quat. Sci. Rev.* **24** (12), 1413-1427 (2005).

214

215 [4] J. H. Curtis, D. A. Hodell, M. Brenner. Climate variability on the Yucatán  
216 Peninsula (Mexico) during the past 3500 years, and implications for Maya cultural  
217 evolution. *Quat. Res.* **46** (1), 37-47 (1996).

218

219 [5] G. H. Haug, D. Günther, L. C. Peterson, D. M. Sigman, K. A. Hughen, B.  
220 Aeschlimann. Climate and the collapse of Maya civilization. *Science* **299**, 1731-35  
221 (2003).

222

223 [6] M. Medina-Elizalde S. J. Burns, D. W. Lea, Y. Asmerom, L. von Gunten, V.  
224 Polyak, M. Vuille, A. Karmalkar. High resolution stalagmite climate record from the  
225 Yucatán Peninsula spanning the Maya Terminal Classic period. *Earth Planet. Sci.*  
226 *Lett.* **298** (1), 255-262 (2010).

227

228 [7] D. J. Kennett, S. F. Breitenbach, V. V. Aquino, Y. Asmerom, J. Awe, J. U.  
229 Baldini, P. Bartlein, B. J. Culleton, C. Ebert, C. Jazwa, M. J. Macri. Development and  
230 disintegration of Maya political systems in response to climate change. *Science* **338**,  
231 788-791 (2012).

232

- 233 [8] D. Wahl, F. Estrada-Belli, L. A. Anderson. 3,400 year paleolimnological record of  
234 prehispanic human–environment interactions in the Holmul region of the southern  
235 Maya lowlands. *Palaeogeogr. Palaeoclimatol. Palaeoecol.* **379–380**, 17–31 (2013).  
236
- 237 [9] P. M. Douglas, M. Pagani, M. A. Canuto, M. Brenner, D. A. Hodell, T. I Eglinton,  
238 J. H. Curtis. Drought, agricultural adaptation, and sociopolitical collapse in the Maya  
239 lowlands. *Proc. Natl. Acad. Sci.* **112** (18), 5607-5612 (2015).  
240
- 241 [10] P. M. Douglas, A. A. Demarest, M. Brenner, M. A. Canuto. Impacts of climate  
242 change on the collapse of lowland Maya civilization. *Annu. Rev. Earth Planet. Sci.*  
243 **44**, 613-645 (2016).  
244
- 245 [11] P. M. Douglas, M. Brenner, J. H. Curtis. Methods and future directions for  
246 paleoclimatology in the Maya lowlands. *Glob. Planet. Change* **138**, 3-24 (2016).  
247
- 248 [12] J. Yaeger, D. A. Hodell. *Climate-culture-environment interactions and the*  
249 *collapse of Classic Maya civilization*. In: D. H. Sandweiss and J. Quilter (Eds.), *El*  
250 *Nino, Catastrophism, and Culture Change in Ancient America*, Dumbarton Oaks, pp.  
251 187-242 (2008).  
252
- 253 [13] M. Medina-Elizalde, E. J. Rohling. Collapse of Classic Maya civilization related  
254 to modest reduction in precipitation. *Science* **335** (6071), 956-959 (2012).  
255
- 256 [14] F. Gázquez, M. Morellón, T. K. Bauska, D. Herwartz, J. Surma, A. Moreno, M.  
257 Staubwasser, B. Valero-Garcés, A. Delgado-Huertas, D. A. Hodell. Triple oxygen and  
258 hydrogen isotopes of gypsum hydration water for quantitative paleo-humidity  
259 reconstruction. *Earth Planet. Sci. Letts.* **481**, 177-188 (2018).  
260
- 261 [15] H. Craig, L. I. Gordon. Deuterium and oxygen 18 variations in the ocean and the  
262 marine atmosphere. Pp. 9–130. In E. Tongiorgi (ed.), *Stable isotopes in*  
263 *oceanographic studies and paleotemperatures*. Consiglio nazionale delle ricerche,  
264 Laboratorio di geologia nucleare, Pisa (1965).

265

266 [16] J. R. Gat. Oxygen and hydrogen isotopes in the hydrologic cycle. *Annu. Rev.*  
267 *Earth Planet. Sci.* **24**, 225–262 (1996).

268

269 [17] D. Herwartz, J. Surma, C. Voigt, S. Assonov, M. Staubwasser. Triple oxygen  
270 isotope systematics of structurally bonded water in gypsum. *Geochim. Cosmochim.*  
271 *Acta* **209**, 254–266 (2017).

272

273 [18] B. Luz, E. Barkan. Variations of  $^{17}\text{O}/^{16}\text{O}$  and  $^{18}\text{O}/^{16}\text{O}$  in meteoric waters.  
274 *Geochim. Cosmochim. Acta* **74**, 6276–6286 (2010).

275

276 [19] J. Surma, S. Assonov, M. J. Bolourchi, M. Staubwasser. Triple oxygen isotope  
277 signatures in evaporated water bodies from the Sistan Oasis, Iran. *Geophys. Res. Lett.*  
278 **42**, 8456–8462 (2015).

279

280 [20] Materials and methods are available as supporting material on *Science Online*.

281

282 [21] Z. Sofer. Isotopic composition of hydration water in gypsum. *Geochim.*  
283 *Cosmochim. Acta* **42**, 1141–1149 (1978).

284

285 [22] D. A. Hodell, A. V. Turchyn, C. J. Wiseman, J. Escobar, J. H. Curtis, M.  
286 Brenner, A. Gilli, A. D. Mueller, F. Anselmetti, D. Ariztegui, E. T. Brown. Late  
287 Glacial temperature and precipitation changes in the lowland Neotropics by tandem  
288 measurement of  $\delta^{18}\text{O}$  in biogenic carbonate and gypsum hydration water. *Geochim.*  
289 *Cosmochim. Acta* **77**, 352–368 (2012).

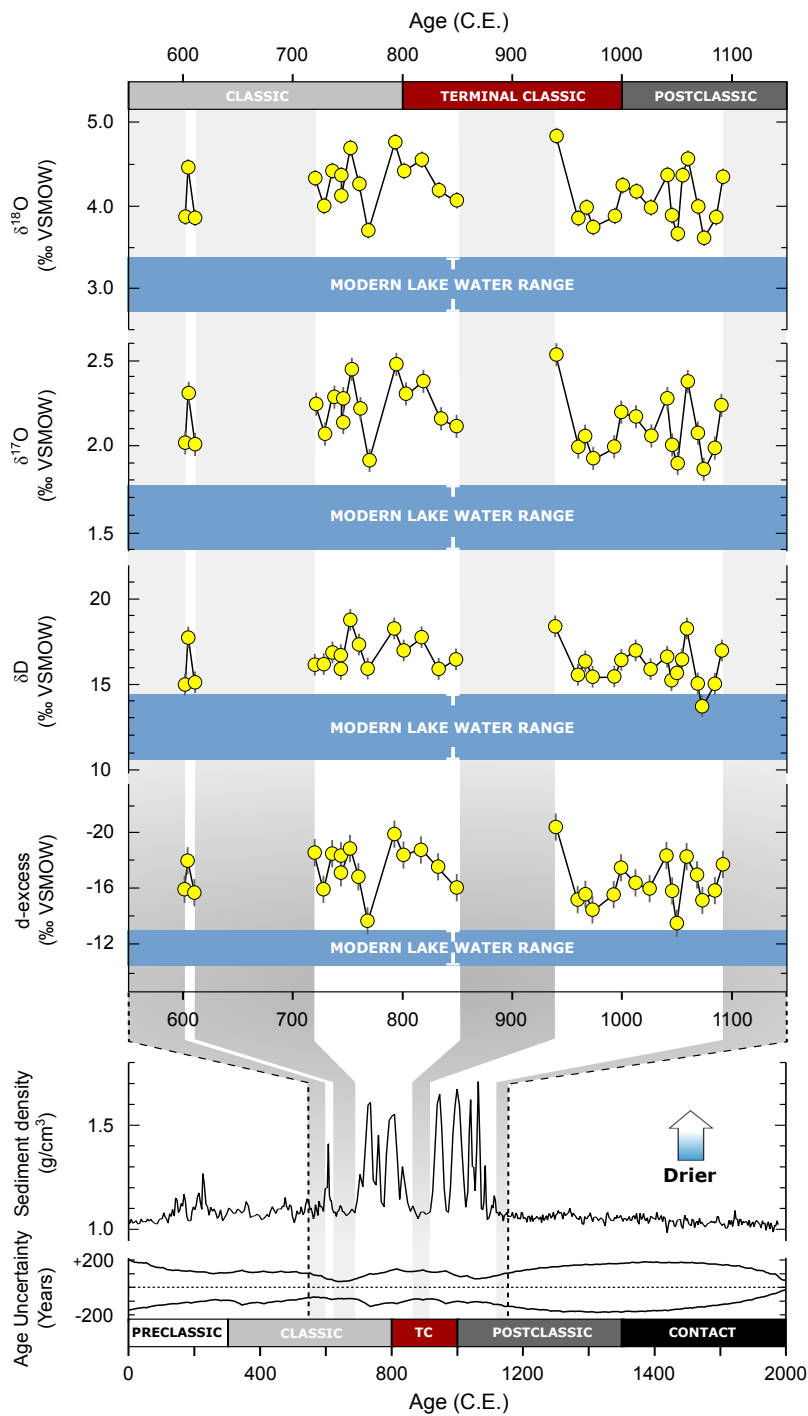
290

291 [23] N. P. Evans, A. V. Turchyn, F. Gázquez, T. R. Bontognali, H. J. Chapman, D. A.  
292 Hodell. Coupled measurements of  $\delta^{18}\text{O}$  and  $\delta\text{D}$  of hydration water and salinity of  
293 fluid inclusions in gypsum from the Messinian Yesares member, Sorbas Basin (SE  
294 Spain). *Earth Planet. Sci. Lett.* **430**, 499–510 (2015).

295

- 296 [24] F. Gázquez, N. P. Evans, D. A. Hodell. Precise and accurate isotope fractionation  
297 factors ( $\alpha^{17}\text{O}$ ,  $\alpha^{18}\text{O}$  and  $\alpha\text{D}$ ) for water and  $\text{CaSO}_4\cdot 2\text{H}_2\text{O}$  (gypsum). *Geochim.*  
298 *Cosmochim. Acta* **198**, 259–270 (2017).  
299
- 300 [25] F. Gázquez, J. M. Calaforra, N. P. Evans, D. A. Hodell. Using stable isotopes  
301 ( $\delta^{17}\text{O}$ ,  $\delta^{18}\text{O}$  and  $\delta\text{D}$ ) of gypsum hydration water to ascertain the role of water  
302 condensation in the formation of subaerial gypsum speleothems. *Chem. Geol.* **452**,  
303 34-46 (2017).  
304
- 305 [26] F. Gázquez, I. Mather, J. Rolfe, N. P. Evans, D. Herwartz, M. Staubwasser, D. A.  
306 Hodell. Simultaneous analysis of  $^{17}\text{O}/^{16}\text{O}$ ,  $^{18}\text{O}/^{16}\text{O}$  and  $^2\text{H}/^1\text{H}$  of gypsum hydration  
307 water by cavity ring-down laser spectroscopy. *Rapid Commun. Mass Spectrom.*  
308 **29**(21), 1997-2006 (2015).  
309
- 310 [27] T. Kluge, H. P. Affek. Quantifying kinetic fractionation in Bunker Cave  
311 speleothems using  $\Delta 47$ . *Quat. Sci. Rev.* **49**, 82–94 (2012).  
312
- 313 [28] M. S. Lachniet. Climatic and environmental controls on speleothem oxygen-  
314 isotope values. *Quat. Sci. Rev.* **28**(5), 412–432 (2009).  
315
- 316 [29] L. I. Wassenaar, S. L. Van Wilgenburg, K. Larson, K. A. Hobson. A  
317 groundwater isoscape ( $\delta\text{D}$ ,  $\delta^{18}\text{O}$ ) for Mexico. *J. Geochem. Explor.* **102**, 123–136  
318 (2009).  
319
- 320 [30] J. A. Hoggarth, M. Restall, J. W. Wood, D. J. Kennett. Drought and its  
321 demographic effects in the Maya lowlands. *Current Anthropology*, **58**(1), 82–113  
322 (2017).

323 **Figures:**

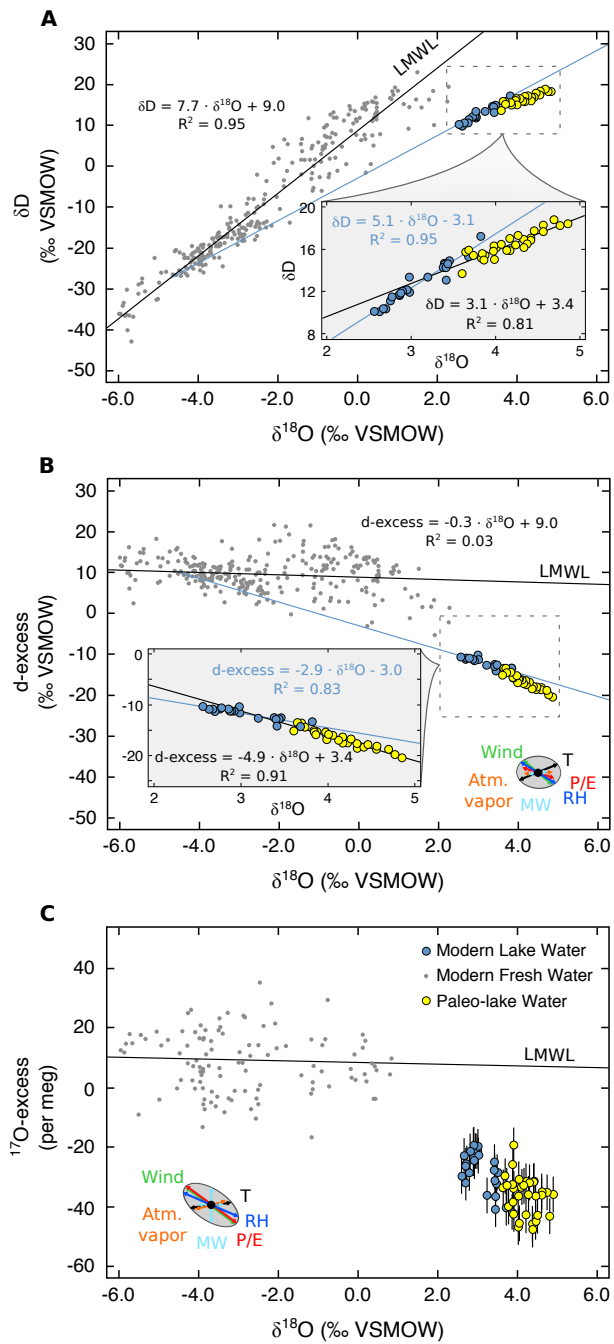


324

325 **Fig. 1:** Water isotopes during drought periods compared to modern water isotopes of  
 326 Lake Chichancanab. **(Lower)** Sediment density record of core CH1 7-III-04 from 0  
 327 to 2000 C.E. (shown relative to Maya chronology) (3). Periods of gypsum  
 328 precipitation are indicated by density values  $>1.1 \text{ g/cm}^3$ . Age uncertainty (95%  
 329 confidence intervals) are derived from Bayesian age-depth analysis and normalized to



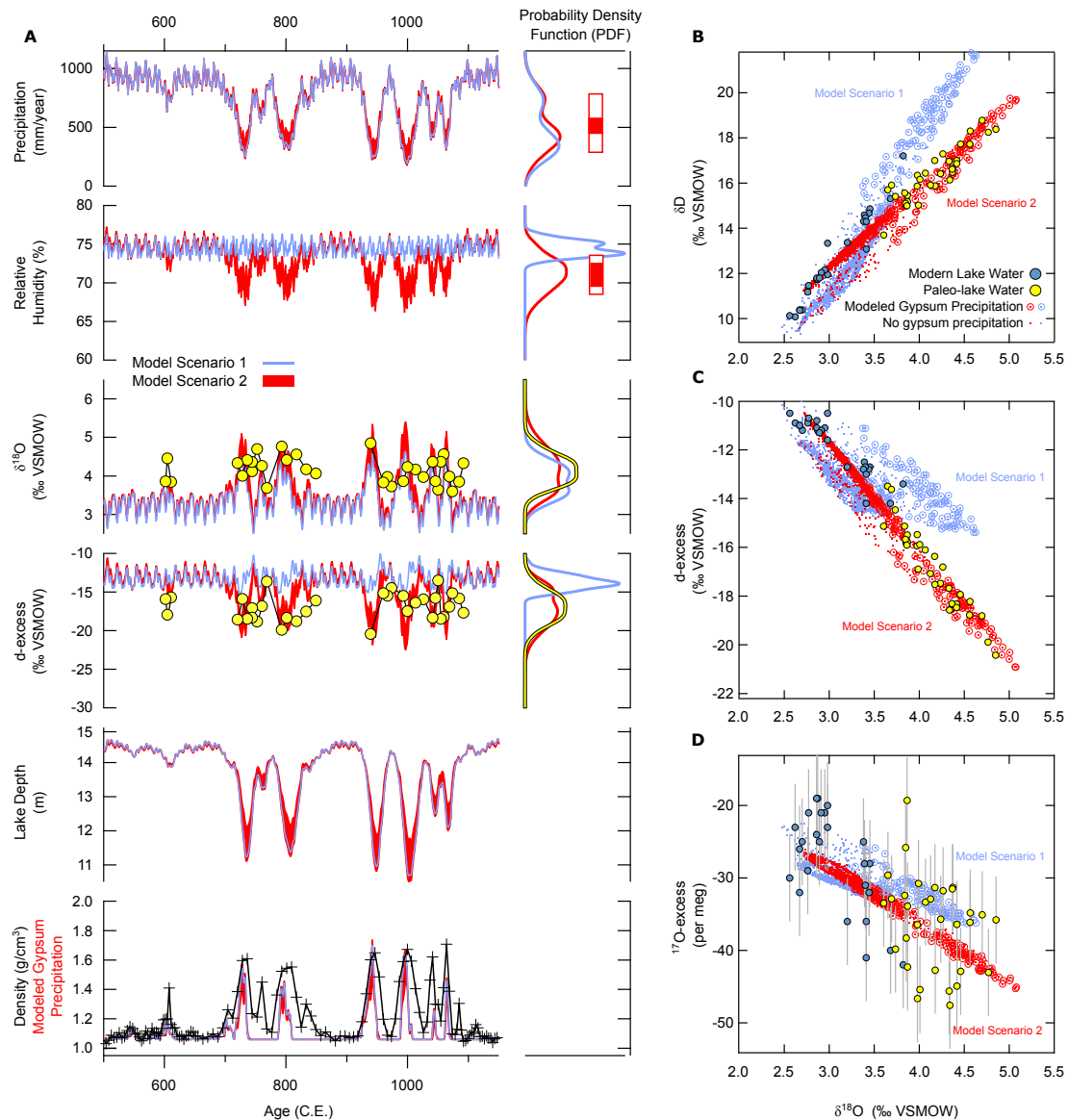
330 the best-fit age model (20) (Fig. S8). (**Upper**)  $\delta^{18}\text{O}$ ,  $\delta^{17}\text{O}$ ,  $\delta\text{D}$  and d-excess ( $\delta\text{D} - 8 \cdot$   
331  $\delta^{18}\text{O}$ ) of paleo-lake water data (yellow circles) from 550 to 1150 C.E shown after  
332 correction of measured GHW for known fractionation factors (24) at 26°C. Horizontal  
333 blue band defines the mean ( $\pm 1\sigma$ ) isotopic composition recorded in the modern lake.  
334 Positive  $\delta^{18}\text{O}$ ,  $\delta^{17}\text{O}$  and  $\delta\text{D}$  values and negative d-excess values reflect periods of  
335 drought. Note d-excess axis is reversed. Abbreviation: VSMOW, Vienna Standard  
336 Mean Ocean Water.



337

338 **Fig. 2:** Comparison of measured local meteoric water (gray circles), modern lake  
 339 water (blue circles) and paleo-lake water data (yellow circles). Paleo-lake water data  
 340 are shown after correction of measured GHW for known fractionation factors (24) at  
 341 26°C. In (A)  $\delta^{18}O$  vs  $\delta D$ , (B)  $\delta^{18}O$  vs d-excess (d-excess =  $\delta D - 8 \cdot \delta^{18}O$ ) and (C)  
 342  $\delta^{18}O$  vs  $^{17}O$ -excess ( $^{17}O$ -excess =  $\ln[\delta^{17}O + 1] - 0.528 \ln[\delta^{18}O + 1]$ ) space, local  
 343 meteoric water measurements define the local meteoric water line (LMWL). Paleo-  
 344 lake water in A, B and C displays greater enrichment along an evaporative trend

345 compared to modern lake waters. The grey ellipses define relative influence of  
346 variables that can affect the isotopic composition of water in  $\delta^{18}\text{O}$  vs d-excess and  
347  $\delta^{18}\text{O}$  vs  $^{17}\text{O}$ -excess space; Precipitation/Evaporation (P/E), normalized relative  
348 humidity ( $\text{RH}_n$ ), temperature (T), changes to source composition (MW), the degree of  
349 equilibrium between atmospheric vapor and fresh water (Atm. vapor), and turbulence  
350 created by wind (Wind) (14). The size of each arrow is derived from the tolerance  
351 given for each input parameter in Table S8.



353

354 **Fig. 3:** (A) Transient model of the lake system from 550 to 1200 C.E. GHW data  
 355 (yellow circles) and core density are plotted against sampling ages derived from  
 356 Bayesian age-depth analysis (20). Multi-decadal-scale droughts were simulated by  
 357 forcing (1) a reduction in precipitation with accompanied shifts in the isotopic  
 358 composition of rainwater (i.e., the amount effect:  $\delta^{18}\text{O}_{\text{precipitation}}/\Delta\text{Precipitation}_{\text{volume}} =$   
 359  $-0.0121\text{‰}/\text{mm}$ ; Scenario 1, blue line) and (2) reductions in precipitation with  
 360 accompanied decreases in  $\text{RH}_n$  (Scenario 2, red field). Probability density functions  
 361 incorporate the variability within and between each decade-long drought (GHW data  
 362 = yellow line; scenario 1 = blue line; scenario 2 = red line). Scenario 1 fails to match

363 the d-excess data derived from GHW. Scenario 2 successfully reproduces all  $\delta^{18}\text{O}$  and  
364 d-excess data. When all model variables were averaged across all droughts, the mean  
365 precipitation and  $\text{RH}_n$  reduction (closed red boxes adjacent to PDFs) is 47% (with a  
366  $1\sigma$  level of 41-54%) and 4% ( $1\sigma$  level 2-7%), respectively. The  $\pm 1\sigma$  range determined  
367 from probability density functions (open red boxes adjacent to PDFs) shows the  
368 variability of precipitation and  $\text{RH}_n$  throughout the droughts. Scenarios 1 and 2 are  
369 also plotted as **(B)**  $\delta^{18}\text{O}$  vs  $\delta\text{D}$ , **(C)**  $\delta^{18}\text{O}$  vs d-excess and **(D)**  $\delta^{18}\text{O}$  vs  $^{17}\text{O}$ -excess.  
370 Open circles indicate points in the model at which gypsum is precipitating; dots  
371 indicate modeled data points when gypsum is not precipitating. Error bars ( $\pm 1\sigma$ ) are  
372 shown or are smaller than the symbols.

373 **Acknowledgments:**

374 We thank James Rolfe for technical assistance and support with stable isotope  
375 measurements, and three anonymous reviewers for insightful comments that  
376 improved the paper. **Funding:** The research leading to these results received funding  
377 from the European Research Council under the European Union's Seventh  
378 Framework Program (FP/2007-2013)/ERC grant agreement n. 339694 (Water  
379 Isotopes of Hydrated Minerals) to D.A.H. **Author Contributions:** D.A.H., N.P.E.  
380 and F.G. developed the analytical method and designed the study. M.B., J.H.C., and  
381 D.A.H. collected the original sediment cores from Lake Chichancanab. N.P.E.  
382 sampled the cores, and N.P.E. and F.G. performed all isotopic analyses. T.K.B.  
383 designed the transient model and performed drought simulations. N.P.E., T.K.B. and  
384 D.A.H. wrote the paper with contributions from all other authors. **Competing**  
385 **Interests:** The authors declare no competing interests. **Data Availability:** All data are  
386 available in the manuscript or supplementary material, and at  
387 [www.ncdc.noaa.gov/paleo/study/24476](http://www.ncdc.noaa.gov/paleo/study/24476).

388

389 **Supporting Online Material:**

390 Materials and Methods

391 Modeling

392 Table S1 – S10

393 Fig S1 – S11

394 References (31 – 54)

395  
396  
397  
398  
399  
400  
401  
402  
403  
404  
405  
406  
407  
408  
409  
410  
411  
412  
413  
414  
415  
416



## Supplementary Materials for

### Quantification of Drought During the Collapse of the Classic Maya Civilization

Nicholas P. Evans\*, Thomas K. Bauska, Fernando Gázquez, Mark Brenner, Jason H. Curtis, and David A. Hodell.

correspondence to: [ne243@cam.ac.uk](mailto:ne243@cam.ac.uk)

**This PDF file includes:**

- Materials and Methods (Section 1.0)
- Modeling (Section 2.0)
- Tables S1 to S10
- Figs. S1 to S11
- References (31 – 54)

417 **1.0 Materials and Methods:**

418

419 **1.1 Sediment Cores and Sampling:**

420

421 Lake Chichancanab is located at  $\sim 19^{\circ}51'21''\text{N}$   $88^{\circ}45'49''\text{W}$ , Yucatán  
422 Peninsula, SE Mexico (Fig. S1). In March 2004, core CH1 7-III-04 was collected  
423 from Lake Chichancanab with a piston corer in 14.7 m of water (3). Shortly after  
424 collection, cores were split, wrapped in plastic film and stored at 4°C. Core sections  
425 were measured for bulk density by gamma-ray attenuation by Hodell et al. (3), and  
426 contain high-density gypsum bands interbedded with low-density organic layers (Fig.  
427 S2). Gypsum was sampled at 0.5 cm intervals – individual crystals were picked from  
428 the  $>350\ \mu\text{m}$  size fraction and ground to a powder. Powdered samples were dried in  
429 an oven at 45°C for 15-20 hours and placed under vacuum ( $\sim 10^{-3}$  mbar) for  $\sim 3$  hours  
430 to remove adsorbed water prior to hydration water extraction (31).

431

432 **1.2 Gypsum Hydration Water (GHW):**

433

434 GHW was extracted from each sample (150-200 mg) by heating to 400°C and  
435 trapping the evolved water, *in vacuo*, using a bespoke offline extraction system  
436 described in Gázquez et al. (26). Triple oxygen ( $^{16}\text{O}$ ,  $^{17}\text{O}$ ,  $^{18}\text{O}$ ) and hydrogen (H, D)  
437 isotopes of the GHW were measured by cavity ring down spectroscopy (CRDS) in the  
438 Godwin Laboratory, University of Cambridge, UK (Table S1), using an L2140-i  
439 Picarro CRDS water isotope analyzer with an attached micro-combustion module  
440 (MCM; Picarro Inc.) (26, 32). The MCM's cartridge was filled with a pyrolytic  
441 catalyst to remove any organic contaminants in the GHW that may spectroscopically  
442 interfere with the CRDS analyses (26). Triple oxygen and hydrogen isotope results  
443 are reported in parts per thousand (‰) relative to V-SMOW. External error ( $1\sigma$ ) was  
444 estimated by repeated analysis ( $n = 11$ ) of an analytical-grade standard extracted  
445 along with the samples (26). Internal standards were calibrated previously against V-  
446 SMOW, GISP, and SLAP for  $\delta^{18}\text{O}$  and  $\delta\text{D}$ , and against V-SMOW and SLAP for  
447  $\delta^{17}\text{O}$ - $\delta^{18}\text{O}$  (33).  $1\sigma$  was  $\pm 0.07\text{‰}$  for  $\delta^{17}\text{O}$ ,  $\pm 0.12\text{‰}$  for  $\delta^{18}\text{O}$ ,  $\pm 0.63\text{‰}$  for  $\delta\text{D}$ ,  $\pm 0.8\text{‰}$   
448 for d-excess and  $\pm 6$  per meg ( $\pm 0.006\text{‰}$ ) for  $^{17}\text{O}$ -excess (Table S2).



449

450 d-excess and  $^{17}\text{O}$ -excess are defined as:

451

$$452 \quad \text{d-excess} = \delta\text{D} - 8 \cdot \delta^{18}\text{O}$$

$$453 \quad ^{17}\text{O-excess} = \ln(\delta^{17}\text{O} + 1) - 0.528 \ln(\delta^{18}\text{O} + 1)$$

454

455 Where 0.528 is the slope of the modern  $\delta^{17}\text{O} - \delta^{18}\text{O}$  Global MWL (34).

456

457 Whereas study of GHW in lakes has produced relevant paleoclimatic records  
458 that agree closely with other local and regional climate proxies (14, 22-24, 35, 36),  
459 GHW can undergo post-depositional isotopic exchange under certain conditions (e.g.  
460 temperature fluctuations  $>60^\circ\text{C}$  during sediment burial and exhumation cycles) (37,  
461 38). We suggest the gypsum in Lake Chichancanab preserves the isotopic composition  
462 of the lake water at the time of deposition and has not undergone post-depositional  
463 diagenesis or exchange with modern lake water. After applying fractionation factors,  
464 the isotopic values of the paleo-lake waters are considerably enriched compared to the  
465 modern lake (Fig. 1; Fig. S2). If the GHW had exchanged with sediment pore water, a  
466 relatively homogeneous isotopic profile, with values similar to the current lake water,  
467 would be expected. What is more, the burial depth of the gypsum is shallow ( $< 2$  m)  
468 and the sediments are porous, thus isotopic gradients in pore water would be strongly  
469 attenuated by diffusion and advection with overlying lake water (14).

470

### 471 **1.3 Precipitation, meteoric and lake water samples:**

472

473 We report the triple oxygen and hydrogen isotopic measurement of lake water  
474 ( $n = 156$ ), river and ground water ( $n = 92$ ), and rainwater ( $n = 31$ ) samples from  
475 stations across the Yucatán Peninsula, collected from 1994 to 2010 (Fig. S10; Tables  
476 S3, S4 and S5). Measurements were made using an L2140-i Picarro CRDS water  
477 isotope analyzer. The majority of rainwater samples were collected at  $20^\circ 00' 59''\text{N}$   
478  $89^\circ 01' 13''\text{W}$ ,  $\sim 30$  km west of Lake Chichancanab (22). All water samples were  
479 collected and stored in Qorpak bottles with Polyseal cone-lined caps to prevent  
480 evaporation.

481

482 **1.4 Biogenic carbonate measurements:**

483

484 Shells and shell fragments of the gastropod *Pyrgophorus coronatus* were  
485 picked from 0.5 cm intervals of core CHI 7-III-04. Shells were cracked and sonicated  
486 in methanol to remove contaminant debris. Subsequently, samples were treated with  
487 10% H<sub>2</sub>O<sub>2</sub> for 30 minutes to remove organic matter, dried and ground to a fine  
488 powder. Stable oxygen isotopes of carbonate were measured using a ThermoScientific  
489 GasBench II, equipped with a CTC autosampler coupled to a MAT253 mass  
490 spectrometer (39). Samples were flushed with CP grade helium then acidified with  
491 104% H<sub>3</sub>PO<sub>4</sub> and reacted at 70°C for 1 hour. Repeat analysis of the Carrara Marble  
492 standard yielded a 1σ analytical precision of ±0.1‰ for δ<sup>18</sup>O. Results are reported  
493 relative to the Vienna Pee Dee Belemnite (VPDB). Small sample fragments were run  
494 on a Kiel III carbonate preparation device interfaced with a Finnigan MAT 252 mass  
495 spectrometer. Analytical precision was estimated at ±0.08‰ for δ<sup>18</sup>O.

496

497 **1.5 Code:**

498

499 All code can be found in the supplementary file  
500 “Evans\_et\_al\_2018\_Matlab\_Model” on *Science* Online. Please address enquiries to  
501 T.K.B. (tkb28@cam.ac.uk).

502

503 **2.0 Modeling:**

504

505 **2.1.1 Transient Model Details:**

506

507 The transient box model presented here is a lake basin with a surface and deep  
508 box (Fig. S4A). The volume (4.57e7 m<sup>3</sup>), surface area (1.02e7 m<sup>2</sup>), and surface area  
509 to depth relationship conform to data presented in Hodell et al. (3) (Fig. S4B). This  
510 geometry equates to a mean depth of 4.5 m in the model with the modern deepest area  
511 of the basin equal to ~15 m.

512

513 The basin is fed by a precipitation flux determined by NARR reanalysis data  
 514 (~1 m water equivalent/m<sup>2</sup>/a; Fig. S5) with a constant catchment size through time.  
 515 The basin hydrology is effectively closed (40). Groundwater flux to and from the lake  
 516 (equivalent to ~10% of precipitation) delivers Ca<sup>2+</sup>, SO<sub>4</sub><sup>-</sup>, Na<sup>2+</sup>, K<sup>+</sup>, Mg<sup>2+</sup> and Cl<sup>-</sup> and  
 517 maintains the lake near the modern salt balance, with gypsum near saturation. Water  
 518 is lost via evaporation, which is held constant at a rate of 1.07 m water  
 519 equivalent/m<sup>2</sup>/a with the absolute flux evolving through time, depending on the  
 520 surface area of the lake.

521

522 The saturation state of gypsum was calculated offline with the PHREEQC  
 523 model for a wide range of solutions, starting at modern conditions. The lake model  
 524 incorporates these solutions in a look-up table to calculate the gypsum saturation at  
 525 every time step. If the lake exceeds saturation, Ca<sup>2+</sup> and SO<sub>4</sub><sup>-</sup> is removed by gypsum  
 526 precipitation at a rate that maintains the lake below saturation, with a response time of  
 527 1 year. Combining the mass of gypsum precipitated and surface area of the lake at a  
 528 given time-step allows us to calculate the gypsum accumulation in the lake sediment.  
 529 This is then used to calculate a synthetic core log of density, assuming the density of  
 530 accumulating gypsum is 2.31 g/cm<sup>3</sup> and that the accumulation of other sediments is  
 531 constant at 0.941 mm/year, with a density of 1.06 g/cm<sup>3</sup> based on the mean sediment  
 532 accumulation that brackets the drought periods.

533

### 534 **2.1.2 Transient Model Isotope and Ionic Mass Balance:**

535

536 The isotope mass balance model employs a Craig-Gordon evaporation scheme  
 537 (15) as formulated in Criss (41). The overall isotopic fractionation during evaporation  
 538 ( $\alpha_{evp}$ ) depends on the equilibrium fractionation ( $\alpha_{eq}$ ), kinetic fractionation ( $\alpha_{kin}$ ),  
 539 relative humidity (h) and the isotopic ratio of water vapor ( $R_v$ ) and the evaporating  
 540 surface of the basin ( $R_b$ ), whereby:

541

$$542 \quad \alpha_{evp} = \alpha_{eq} \alpha_{kin} \left( \frac{1 - h}{1 - \alpha_{eq} h \frac{R_v}{R_b}} \right) \quad (1)$$

543

544 Equilibrium fractionation ( $\alpha_{eq}$ ) for  $H_2O^{18}$  ( $\alpha^{18}O_{eq}$ ) and DHO ( $\alpha D_{eq}$ ) are  
545 calculated using an assumed lake surface temperature of 25°C and the equations of  
546 Horita and Wesolowski (42). The equilibrium fractionation for  $H_2O^{17}$  is then a  
547 function  $\alpha^{18}O_{eq}$ , where:

548

549

$$\alpha^{17}O_{eq} = \alpha^{18}O_{eq}^{\theta_{eq}}$$

550

551 and  $\theta_{eq}$  is 0.529 (43).

552

553 Kinetic fractionation factors for all three minor isotopes are calculated as a  
554 function of wind-induced turbulence ( $w$ ), lake surface temperature ( $T$ ) and the kinetic  
555 fractionation parameter between  $^{18}O$  and  $^{17}O$  ( $\theta_{kin}$ ):

556

557

$$\alpha^{18}O_{kin} = 1.0283^w$$

558

$$\alpha D_{kin} = (1.25 - 0.02T)(\alpha^{18}O_{kin} - 1) + 1$$

559

$$\alpha^{17}O_{kin} = \alpha^{18}O_{kin}^{\theta_{kin}}$$

560

561 We assume  $R_v$  depends on the degree to which the atmospheric water vapor  
562 ( $v_{eq}$ ) is in equilibrium with  $R_p$  (44) where:

563

564

$$R_v = R_p(\alpha_{eq(p-v)}V_{eq})$$

565

566 The general form of the mass-balance equation for the mass of a given species ( $mX$ )  
567 of either isotope or ion in basin box 1 (b1) is:

568

569

$$\frac{dmX_{b1}}{dt} = F_p R_p - F_{evp} R_{evp} + F_{gb1} R_g - F_{b1g} R_{b1} + F_{b2b1} R_{b2} - F_{b1b2} R_{b1}$$

570

571 Similarly the mass balance for basin box 2 (b2) is:

572

573 
$$\frac{dmX_{b2}}{dt} = F_{b1b2}R_{b1} - F_{b2b1}R_{b2}$$

574

575 In this set of equations F represents the various fluxes of water in terms of mass of the  
 576 major water isotope (HHO<sup>16</sup>) and R represents the ratio of minor isotope or ionic  
 577 species relative to HHO<sup>16</sup>. As examples, the ratio of deuterium in box 1 is:

578

579 
$$R_{DHO,b1} = \frac{mDHO_{b1}}{mHHO^{16}_{b1}}$$

580

581 The concentration of Ca in box 1 is:

582

583 
$$R_{[Ca],b1} = \frac{mCa_{b1}}{mHHO^{16}_{b1}}$$

584

585 When the overall water mass balance is calculated (i.e. the variation in volume):

586

587 
$$R_{HHO^{16},b1} = 1$$

588

589 Ratios for external isotopic such as the precipitation and groundwater fluxes are  
 590 referenced relative to VSMOW such that:

591

592 
$$R_{DHO,p} = \left( \frac{\delta D_p}{10^3} + 1 \right) R_{DHO,VSMOW}$$

593

594 The isotopic ratios of the evaporation flux ( $R_{evp}$ ) are determined from Equation 1 and  
 595 the isotopic ratios of the basin surface ( $R_{b1}$ ):

596

597 
$$R_{evp} = \frac{R_{b1}}{\alpha_{evp}}$$

598

### 599 2.1.3 Transient Model Parameterization:

600

601 When modeling the isotopic composition of the paleo-lake, the (1) lake  
602 surface temperature (T), (2) wind-induced turbulence (w), (3) isotopic composition of  
603 the atmospheric vapor, (4) salinity effect on isotope fractionation, and (5) the isotopic  
604 composition of the freshwater input (and any variability caused by the amount effect)  
605 must be known or assumed (Table S6).

606

607 1. To constrain water temperature changes at Lake Chichancanab during the  
608 Terminal Classic Period (TCP), tandem measurements of both gypsum  
609 hydration water (GHW) and carbonate  $\delta^{18}\text{O}$  that were deposited concurrently  
610 permit the deconvolution of the  $\delta^{18}\text{O}$  carbonate signal into its temperature and  
611  $\delta^{18}\text{O}$ -water components via the carbonate paleo-temperature equation (22). To  
612 calculate the temperature at which the aragonitic shells of *Pyrgophorus*  
613 *coronatus* formed, we used the equation of Grossman and Ku (45) that is  
614 based on analysis of foraminifera (*Hoeglundina elegans*) and gastropods:

615

$$616 \quad T \text{ } ^\circ\text{C} = 21.8 - 4.59(\delta^{18}\text{O}_{\text{arag PDB}} - \delta^{18}\text{O}_{\text{water SMOW}})$$

617

618 The  $\delta^{18}\text{O}$  of gastropod aragonite and GHW is used to estimate  $\delta^{18}\text{O}_{\text{arag}}$  and  
619  $\delta^{18}\text{O}_{\text{water}}$ , respectively. Gypsum and gastropod samples were only used if they  
620 were in direct contact with each other, or the shell fragments were found  
621 embedded within gypsum. The derived temperature from *Pyrgophorus*  
622 *coronatus* and gypsum from the same bed averaged  $25.9 \pm 1.7^\circ\text{C}$  (Table S7).  
623 This temperature is indistinguishable from the mean annual temperature of the  
624 lake today (22). Equally, because  $^{17}\text{O}$ -excess is minimally affected by  
625 temperature changes, moderate variations in mean temperature result in  
626 insignificant effects on the trajectories of the evaporated waters. For example,  
627  $5^\circ\text{C}$  of temperature change has a small effect on the model results for  $^{17}\text{O}$ -  
628 excess (up to  $\sim \pm 2$  per meg in a terminal lake), whereas d-excess changes by as  
629 much as  $\sim 3\text{‰}$  in a terminal lake, when all other parameters remain constant  
630 (14). Thus, the model sensitivity to temperature changes is low.

631

632 2. It is known that the proportion of  $\alpha^{18}\text{O}_{\text{kin}}$  may be suppressed by turbulent flow  
633 induced by wind (46), and therefore wind could alter isotope mass balance,  
634 especially for d-excess and  $^{17}\text{O}$ -excess. The exponent 'w' is set between 0.5  
635 (pure turbulence) and 1 (no wind). Measured wind speeds in the region of  
636 Lake Chichancanab are  $\sim 3$  m/s and relatively constant over the year (47),  
637 resulting in a well-mixed lake-surface layer. When turbulence is not  
638 considered, the model yields d-excess and  $^{17}\text{O}$ -excess values that are  
639 systematically too low compared to the analytical data for some modern  
640 periods. We also tested this variable by analyzing modern and paleo-lake  
641 water data using previously published Monte Carlo models (14) (Section  
642 2.1.5). These tests provide the best fit to modeled data when w is kept constant  
643 at  $\sim 0.5$  when modeling both the modern and the TCP GHW data.

644

645 3. The isotopic composition of modern atmospheric vapor is not well constrained  
646 in the Yucatán Peninsula, nor are there estimates available for how this  
647 variable has changed in the past. Assuming equilibrium with local meteoric  
648 water, the isotopic composition of atmospheric water vapor can be  
649 approximated (14). Gibson et al. (44), however, suggested that the isotopic  
650 composition of atmospheric vapor is often only in partial equilibrium with that  
651 of local freshwater. We assumed a degree of equilibrium of 60%, a reasonable  
652 estimate for most tropical and inter-tropical regions (44). Note that Gázquez et  
653 al. (14) show that the triple oxygen and hydrogen system is relatively sensitive  
654 to the isotopic composition of the vapor, especially for coastal lakes affected  
655 by advection of marine vapor masses. In coastal lakes, the isotopic  
656 composition of the modern atmospheric vapor is in equilibrium with seawater  
657 rather than freshwater. This is probably not the case at Lake Chichancanab,  
658 which is located  $\sim 140$  km inland.

659

660 4. High concentrations of NaCl and other salts within a lake can cause the water  
661 isotopic activity ratios to diverge from the corresponding concentration ratios,  
662 as a consequence of isotopic fractionation between free water and water in

663 ionic hydration shells (17, 48). This “salt effect” is different for hydrogen and  
664 oxygen isotope fractionation, resulting in complications when interpreting the  
665 relationship between  $\delta^{18}\text{O}$  and  $\delta\text{D}$  at salt concentrations  $>100,000$  mg/L (17,  
666 48). The total dissolved salt concentration in Lake Chichancanab today is  
667  $\sim 4000$  mg/L (3). Substantial oxygen and hydrogen isotope fractionation effects  
668 caused by high salinity would not be expected at these low concentrations (41,  
669 48). During periods of lake drawdown, the transient model displays elevated  
670 salt concentrations, but concentrations that approach 100,000 mg/L are never  
671 experienced in model runs.

672

673 5. The mean ( $\pm 1\sigma$ ) modern isotopic composition of regional groundwater is  $-4.0$   
674  $\pm 1.7\text{‰}$  for  $\delta^{18}\text{O}$ ,  $-2.10 \pm 0.9\text{‰}$  for  $\delta^{17}\text{O}$  and  $-23.5 \pm 12.8\text{‰}$  for  $\delta\text{D}$ . We used  
675  $\delta^{18}\text{O} = -4.5\text{‰}$  and  $\delta\text{D} = -26\text{‰}$  (so that d-excess = 10‰) and set  $^{17}\text{O}$ -excess =  
676 2.5 per meg to model present-day conditions. These variables were held  
677 constant throughout the transient model runs, although they can be  
678 systematically varied to reflect isotope effects such as the amount effect (see  
679 below and Section 2.1.4). We tested the effect of non-systematic variability on  
680 the isotopic composition of meteoric water (using bounds of  $\pm 0.5\text{‰}$  for  $\delta^{18}\text{O}$ ,  
681  $\pm 5\text{‰}$  for d-excess, and  $\pm 9.5$  per meg for  $^{17}\text{O}$ -excess), using the steady state  
682 Monte Carlo model of Gázquez et al. (14) to quantify derived uncertainty  
683 (Section 2.1.5).

684

685 The amount effect (i.e. correlation between depletion of heavy isotopes in  
686 rainfall with greater amount of rain) is thought to play a role in the Yucatán  
687 Peninsula and thus the isotopic composition of meteoric water may vary over  
688 the timescales modeled (6, 13). The amount effect and its perturbation in the  
689  $\delta^{18}\text{O}$  of precipitation (P) over a seasonal cycle was calculated from isotopic  
690 composition of precipitation collected at  $20^{\circ}00'59''\text{N}$   $89^{\circ}01'13''\text{W}$  (22), and  
691 rainfall amounts from the proximal meteorological station at Dziuche,  
692  $19^{\circ}54'00''\text{N}$   $88^{\circ}48'40''\text{W}$ , from 2006 to 2009. The linear regression ( $\delta^{18}\text{O} = -$   
693  $0.0176(\text{P}) - 0.1204$ ;  $R^2 = 0.92$ ) is very similar to that found by Medina-  
694 Elizalde et al. (6) from the IAEA station in Veracruz, México ( $\delta^{18}\text{O} = -$



695 0.0118(P) - 0.64;  $R^2 = 0.80$ ). We compiled data from Veracruz between 1969  
696 and 1985 (omitting years with poor data coverage) and the records from  
697 Chichancanab between 2006 and 2009 (22). The compiled linear regression for  
698  $\delta^{18}\text{O}$  ( $\delta^{18}\text{O} = -0.0121(\text{P}) - 0.41$ ) displays a significant correlation ( $R^2 = 0.73$ ),  
699 whereas there was no significant amount effect displayed by d-excess or  $^{17}\text{O}$ -  
700 excess (Fig. S7).

701

#### 702 **2.1.4 Deconvolution of climatic variables:**

703

704  $\delta^{18}\text{O}$ ,  $^{17}\text{O}$ -excess and d-excess are affected to differing degrees by changes in  
705  $\text{RH}_n$ , the ratio P/E, temperature, turbulence (e.g., wind) on the water surface during  
706 evaporation, the isotopic composition of the atmospheric water vapor, changes to the  
707 isotopic composition of the input source (14, 19, 41, 44). In  $\delta^{18}\text{O}$ - $^{17}\text{O}$ -excess and  
708  $\delta^{18}\text{O}$ -d-excess space, the predicted trends of waters undergoing evaporation (in partial  
709 equilibrium with atmospheric vapor) show that  $^{17}\text{O}$ -excess and d-excess are largely  
710 sensitive to  $\text{RH}_n$  and the ratio P/E, moderately sensitive to the isotopic composition of  
711 freshwater input, turbulence on the water surface during evaporation and to the  
712 isotopic composition of the atmospheric water vapor, whereas their sensitivities to  
713 temperature are relatively small, especially for  $^{17}\text{O}$ -excess (Fig. 2) (14). Because the  
714 isotopic composition of the freshwater input, along with variance in the turbulence on  
715 the water surface during evaporation, the isotopic composition of the atmospheric  
716 water vapor, and temperature are relatively well constrained (Section 2.1.3; Table S6),  
717 variability in  $\text{RH}_n$ , P/E and changes in the isotopic composition of the freshwater  
718 input (caused by the amount effect) can be deconvolved in model scenarios.

719

720 To provide semi-realistic scenarios that are directly comparable to the GHW  
721 data, transient simulations were run in which NARR precipitation and  $\text{RH}_n$  forcings  
722 were reduced by variable amounts to simulate a series of multi-decadal-scale droughts  
723 (Fig. 3; Fig. S3). Precipitation and/or  $\text{RH}_n$  forcings are directly modulated by the  
724 density record of core CH1-III-04 (3); the maximum variability during a run was set  
725 to the maximum density point over time, and precipitation and/or  $\text{RH}_n$  were reduced  
726 linearly across all months. Absolute reductions in P/E and  $\text{RH}_n$  were referenced

727 relative to mean NARR data over the period from 1994 to 2010. In other words, a  
728 50% reduction in precipitation and a 5% reduction in  $RH_n$  would equate to 50% less  
729 rainfall in each month (e.g. 200mm/mth to 100mm/mth), and a decrease in the  
730 absolute  $RH_n$  by 5 percentage units each month (e.g.  $RH_n = 75\%$  to  $RH_n = 70\%$ )  
731 during a modeled time period compared to the 1994 to 2010 baseline.

732

733 During model runs, the intervals of modeled gypsum accumulation were first  
734 selected from a pre-determined density range (modeled sediment density  $>1.1 \text{ g/cm}^3$ ).  
735 The periods of modeled gypsum accumulation were then aggregated into drought  
736 conditions for a given scenario in two ways: (i) all model variables were averaged  
737 across all the droughts, and (ii) probability density functions were constructed  
738 incorporating the variability within and between each decadal-length drought (Fig.  
739 S3). To identify the timing of significant gypsum accumulation, we selected periods  
740 of modeled sediment density  $>1.2 \text{ g/cm}^3$ . This would be equivalent to selecting data  
741 outside one standard deviation of the mean sediment density from core CH1-III-04  
742 ( $1.09 \pm 0.11 \text{ g/cm}^3$ ), calculated from the total sediment density record of Hodell et al.  
743 (3) from 500 B.C. to 2000 C.E. (Fig. S6A). Modeled data from these periods were  
744 then compared to mean ( $\pm 1\sigma$ ) GHW data. The model runs were selected as positive  
745 when the modeled  $\delta^{18}\text{O}$ , d-excess and  $^{17}\text{O}$ -excess (during periods of significant  
746 gypsum precipitation) fell within one standard deviation ( $1\sigma$ ) of the GHW data (Fig.  
747 S6). A major constraint on the modeled P/E variability is the sediment density range  
748 from which the modeled data are selected. As displayed in Fig. S6, if the modeled  
749 sediment density threshold is changed from  $1.2 \text{ g/cm}^3$ , the lower bound of P/E and  
750  $RH_n$  estimates will vary systematically. Importantly, increasingly conservative  
751 estimates for periods of gypsum precipitation (i.e. modeled sediment density  $>1.2$   
752  $\text{g/cm}^3$ ) produce increasingly more severe reductions in baseline P/E and  $RH_n$ .

753

754 Two scenarios were tested: (i) a reduction in precipitation with accompanying  
755 shifts in the isotopic composition of rainwater (i.e. the amount effect) and, (ii) a  
756 reduction in precipitation with accompanying decreases in  $RH_n$ . In scenario 1 (main  
757 text; Fig. 3), the density record modulates changes in the P/E ratio. Modeled  
758 precipitation  $\delta^{18}\text{O}$  was simultaneously varied according to the amount effect

759 relationship (i.e.  $\delta^{18}\text{O}_{\text{precipitation}}/\Delta\text{Precipitation}_{\text{volume}} = -0.0121\%/mm$ ; Fig. S7). As the  
760 associated changes in  $\delta\text{D}$  and  $\delta^{17}\text{O}$  track the Global MWL, no changes in d-excess or  
761  $^{17}\text{O}$ -excess are imposed in these scenarios. No scenarios were able reproduce the  
762 relationship between  $\delta^{18}\text{O}$ , d-excess and  $^{17}\text{O}$ -excess observed in the data. In scenario  
763 2, changes in the ratio P/E were coupled with changes to  $\text{RH}_n$ .

764

765 It should also be noted that a combination of  $\text{RH}_n$  reduction and the amount  
766 effect could potentially reproduce the observed data during the TCP. Although a  
767 combination of  $\text{RH}_n$  reduction and (a suppressed) amount effect cannot be definitively  
768 ruled out, given the great number of possible outcomes when modeling three variable  
769 parameters, our experiments show that the amount effect does not dominate the  
770 isotopic budget of the lake. Thus, any influence of the amount effect (in combination  
771 with  $\text{RH}_n$  reductions) at Lake Chichancanab during the TCP will have little effect on  
772 modeled outcomes because of the dominance of  $\text{RH}_n$  in the  $^{17}\text{O}$ -excess and d-excess  
773 signal.

774

### 775 **2.1.5 Monte Carlo Modeling Scenarios:**

776

777 In addition to transient model experiments described above and in the main  
778 body of the text, we also used a previously described steady state model of the lake in  
779 a series of Monte Carlo experiments to determine the range of climatological  
780 conditions that simultaneously satisfy all stable isotope results of GHW, in  
781 combination with statistical estimates of uncertainty (Fig. S9) (14). In these scenarios,  
782 the parameter “Xe” represents the hydrologic balance of the lake. A scenario in which  
783 all water is lost by outflow and no evaporation occurs is represented as  $\text{Xe} = 0$ ,  
784 whereas a scenario in which all water is lost to evaporation (i.e. a terminal basin) is  
785 represented as  $\text{Xe} = 1$ . The Xe of Lake Chichancanab is not believed to have changed  
786 over the last ~1500 years and near-terminal conditions are thought to have prevailed  
787 (40). Equally, Gázquez et al. (14) show that when Xe ranges from 0.75 to 1, changes  
788 in this parameter barely affect the  $\text{RH}_n$  values derived from this Monte Carlo model.  
789 Here, we chose conservative estimates of Xe between 0.8 and 0.9 to cover all likely  
790 variability (Table S8).

791

792 Modeled GHW data suggest there was a reduction in  $RH_n$  of between 2 and  
793 9% during the TCP, compared to the period when modern lake water was sampled  
794 (1994-2010), in good agreement with our transient experiments (2-7%) (Table S9).  
795 Estimated errors for  $RH_n$  are smaller than 4% ( $1\sigma$ ) when all variables listed in Table  
796 S8 are considered. The slightly greater estimates for reductions in  $RH_n$  relative to the  
797 transient model arise because the steady-state assumption in the Monte Carlo model  
798 precludes an accurate simulation of isotopic balance during lake level fluctuations.  
799 Because the model does not account for the additional isotopic enrichment in the lake  
800 due to decreased P/E during a lake-level drawdown, it is slightly biased towards  
801 higher estimates of  $RH_n$  reduction.

802

## 803 **2.2 Age Models:**

804

805 Radiocarbon ages for core CH1 7-III-04 were obtained by Hodell et al. (3).  
806 We estimated calendar ages with 95% confidence intervals using the Bayesian Age-  
807 Depth Modeling software “BACON” in R (Fig. S8) (49). Derived age-depth error  
808 (95% confidence intervals) was normalized to the best-fit line to produce age-depth  
809 errors for the Chichancanab density record (3) (Fig. 1; Table S10). To quantify age  
810 uncertainty in relation to the timing of dry intervals, we inverted the density record of  
811 core CH1-III-04 and identified data outside one standard deviation of the mean  
812 sediment density from core CH1-III-04. This would be equivalent to selecting  
813 sediment densities  $>1.2 \text{ g/cm}^3$ , equivalent to the periods from which GHW was  
814 extracted. The BACON function ‘Events’ was then used to quantify the probability of  
815 arid conditions at any calendar age. Fifty-year window widths were used, with the  
816 windows moving at 10-year steps from the core's bottom ages to its top (Fig. S11)  
817 (49).

818

819 We also used Bayesian age modeling techniques to synthesize the regional  
820 proxy records of Curtis et al. (4), Wahl et al. (8) and Douglas et al. (50) (Fig. S11). To  
821 quantify age uncertainty in relation to the timing of dry intervals, we inverted the  
822 records and identified the lowest 10th percentile of the raw data for Wahl et al. (8)

823 and Douglas et al. (50), and the 5-point smooth of the  $\delta^{18}\text{O}$  *Cytheridella ilosvayi*  
824 record from Curtis et al. (4).

825

826 All proxy records dated using radiometric techniques yielded a significant age  
827 uncertainty. Overall, although individual records show subtle variations in drought  
828 timing, the age uncertainty results in the chance of drought occurring any time  
829 between 500 and 1300 C.E. (51). Gypsum deposition at Lake Chichancanab displays a  
830 significant chance of occurring from ~750 to ~850 C.E (Probability of drought at 800  
831 C.E. = 0.85), coinciding with the onset of the collapse of Terminal Classic Maya  
832 Civilization (Fig. S11).

833 **Supplementary Tables:**

834

835 **Table S1:**

836 Isotopic composition of measured gypsum hydration water (GHW) and calculated  
 837 lake mother water (MW) from samples recovered from core CH1 7-III-04, Lake  
 838 Chichancanab. Asterisk denotes samples that were analyzed with the MCM of the  
 839 L2140-i Picarro CRDS turned off;  $\delta^{17}\text{O}$  results were considered unreliable (26) and  
 840 samples were not used in modeling analysis.

841

Sample name	Age (A.D.)	$\delta^{17}\text{O}$ (GHW)	$\delta^{18}\text{O}$ (GHW)	$\delta\text{D}$ (GHW)	$\delta^{17}\text{O}$ (MW)	$\delta^{18}\text{O}$ (MW)	$\delta\text{D}$ (MW)	$^{17}\text{O}$ -excess (MW)	d-excess (MW)	
<b>A</b>										
CHI 07-III-04 128.0-128.5 cm	1092	4.08	7.81	-2.66	2.24	4.33	17.0	-46	-17.7	
CHI 07-III-04 129.0-129.5 cm	1085	3.83	7.33	-4.58	1.99	3.85	15.0	-38	-15.8	
CHI 07-III-04 130.5-131.0 cm	1073	3.70	7.08	-5.86	1.87	3.60	13.7	-33	-15.1	
CHI 07-III-04 130.5-131.0 cm*	1073		6.95	-5.69		3.48	13.9		-14.0	
CHI 07-III-04 131.0-131.5 cm	1069	3.91	7.46	-4.57	2.07	3.99	15.0	-31	-16.9	
CHI 07-III-04 132.0-132.5 cm	1059	4.21	8.04	-1.35	2.37	4.57	18.3	-35	-18.2	
CHI 07-III-04 132.5-133.0 cm*	1055		7.84	-3.14		4.37	16.5		-18.5	
CHI 07-III-04 133.0-133.5 cm	1050	3.73	7.12	-3.90	1.90	3.65	15.7	-30	-13.5	
CHI 07-III-04 133.5-134.0 cm	1046	3.84	7.34	-4.41	2.01	3.87	15.2	-34	-15.8	
CHI 07-III-04 133.5-134.0 cm	1046		7.20	-4.42		3.72	15.2		-14.6	
CHI 07-III-04 134.0-134.5 cm	1041	4.11	7.85	-2.99	2.27	4.37	16.6	-31	-18.3	
CHI 07-III-04 134.0-134.5 cm*	1041		7.58	-3.29		4.10	16.3		-16.5	
CHI 07-III-04 135.5-136.0 cm	1026	3.90	7.45	-3.74	2.06	3.98	15.9	-36	-15.9	
CHI 07-III-04 136.0-136.5 cm	1013	4.01	7.65	-2.63	2.17	4.17	17.0	-31	-16.4	
CHI 07-III-04 136.5-137.0 cm	1000	4.04	7.71	-3.20	2.20	4.24	16.4	-36	-17.5	
CHI 07-III-04 137.0-137.5 cm	993	3.83	7.34	-4.14	2.00	3.87	15.5	-42	-15.5	
CHI 07-III-04 139.5-140.0 cm	973	3.77	7.21	-4.19	1.93	3.73	15.4	-40	-14.5	
CHI 07-III-04 139.5-140.0 cm*	973		7.55	-2.21		4.07	17.4		-15.1	
CHI 07-III-04 140.0-140.5 cm	967	3.89	7.45	-3.27	2.05	3.98	16.3	-47	-15.5	
CHI 07-III-04 140.5-142.5 cm*	960		7.47	-3.50		3.99	16.1		-15.8	
CHI 07-III-04 140.5-141.5 cm	960	3.83	7.31	-4.04	1.99	3.84	15.6	-32	-15.1	
CHI 07-III-04 142.0-142.5 cm	939	4.36	8.33	-1.27	2.52	4.85	18.4	-36	-20.4	
CHI 07-III-04 142.0-142.5 cm*	939		8.14	-1.50		4.66	18.2		-19.2	
<b>B</b>										
CHI 07-III-04 148.0-148.5 cm	849	3.95	7.54	-3.18	2.11	4.07	16.4	-33	-16.1	
CHI 07-III-04 148.5-149.0 cm*	841		7.71	-3.50		4.24	16.1		-17.8	
CHI 07-III-04 149.0-149.5 cm	833	4.00	7.65	-3.72	2.16	4.18	15.9	-43	-17.5	
CHI 07-III-04 150.0-151.0 cm	817	4.21	8.04	-1.92	2.37	4.56	17.7	-36	-18.8	
CHI 07-III-04 151.0-151.5 cm	801	4.13	7.89	-2.62	2.29	4.42	17.0	-36	-18.3	
CHI 07-III-04 151.5-152.0 cm	793	4.31	8.24	-1.40	2.47	4.77	18.2	-43	-19.9	
CHI 07-III-04 153.0-153.5 cm	768	3.75	7.17	-3.70	1.91	3.69	15.9	-33	-13.6	
CHI 07-III-04 153.0-153.5 cm*	768		7.54	-2.40		4.07	17.2		-15.3	
CHI 07-III-04 153.5-154.0 cm	760	4.05	7.74	-2.34	2.22	4.26	17.3	-32	-16.8	
CHI 07-III-04 154.0-154.5 cm	752	4.28	8.18	-0.88	2.44	4.70	18.8	-35	-18.8	
CHI 07-III-04 154.0-154.5 cm*	752		8.25	0.43		4.77	20.1		-18.1	
CHI 07-III-04 154.5-155.0 cm	744	3.98	7.60	-3.69	2.14	4.12	15.9	-33	-17.1	
CHI 07-III-04 154.5-155.0 cm	744	4.11	7.84	-3.01	2.27	4.37	16.6	-32	-18.3	
CHI 07-III-04 155.0-155.5 cm	736	4.12	7.89	-2.76	2.28	4.42	16.9	-45	-18.5	
CHI 07-III-04 155.5-156.0 cm	728	3.90	7.48	-3.44	2.07	4.01	16.2	-45	-15.9	
CHI 07-III-04 156.0-156.5 cm	720	4.08	7.81	-3.47	2.24	4.34	16.1	-48	-18.6	
<b>C</b>										
CHI 07-III-04 166.0-166.5 cm	611	3.84	7.32	-4.48	2.00	3.85	15.1	-26	-15.7	
CHI 07-III-04 167.0-167.5 cm	605	4.15	7.93	-1.91	2.31	4.46	17.7	-43	-17.9	
CHI 07-III-04 167.5-168.0 cm	602	3.86	7.34	-4.59	2.02	3.86	15.0	-19	-15.9	

842

843 **Table S2:**

844 External and internal reproducibility of GHW measurements.

EXTERNAL PRECISION	$\delta^{17}\text{O}$	$\delta^{18}\text{O}$	$\delta\text{D}$	$^{17}\text{O}$ -excess	d-excess
NEWGYP L6 27/8/15	0.21	0.37	-49.78	12	-52.3
NEWGYP L6 9/9/15	0.28	0.50	-51.34	22	-55.3
NEWGYP L6 29/4/16	0.14	0.23	-51.11	14	-52.8
NEWGYP L4 4/5/16	0.30	0.52	-50.81	23	-54.5
NEWGYP L3 5/5/16	0.29	0.49	-51.27	25	-55.2
NEWGYP L4 11/5/16 (1)	0.21	0.36	-50.80	18	-53.7
NEWGYP L5 12/5/16	0.08	0.14	-51.81	10	-52.9
NEWGYP L6 13/5/16	0.17	0.30	-51.77	10	-54.2
NEWGYP L1 10/6/16 (1)	0.19	0.31	-50.78	22	-53.3
NEWGYP L2 11/6/16 (2)	0.17	0.31	-51.88	9	-54.4
NEWGYP L4 17/8/16	0.20	0.35	-50.59	16	-52.9
<b>1<math>\sigma</math></b>	<b>0.07</b>	<b>0.12</b>	<b>0.63</b>	<b>6</b>	<b>1.0</b>

INTERNAL PRECISION	$\delta^{17}\text{O}$	$\delta^{18}\text{O}$	$\delta\text{D}$	$^{17}\text{O}$ -excess	d-excess
SPIT	-0.07	-0.12	-0.66	-8	0.3
SPIT	0.03	0.06	0.44	0	0.0
SPIT	0.03	0.08	0.63	-11	0.0
SPIT	-0.02	-0.02	0.76	-11	0.9
SPIT	-0.06	-0.09	-0.75	-14	0.0
SPIT	0.03	0.06	-0.01	-3	-0.5
SPIT	0.02	0.05	-0.66	-5	-0.8
SPIT	0.05	0.12	-0.09	-9	-1.1
SPIT	0.04	0.06	-0.04	4	-0.6
SPIT	-0.08	-0.14	-0.60	-5	0.9
SPIT	0.01	-0.01	-1.65	13	-1.6
SPIT	0.02	0.04	0.32	-1	0.0
SPIT	-0.06	-0.11	-0.65	-4	0.2
SPIT	0.01	0.02	0.09	-5	-0.1
SPIT	0.06	0.11	0.26	-2	-0.6
SPIT	0.00	-0.01	-1.03	3	-1.0
SPIT	-0.08	-0.15	-0.60	1	1.1
SPIT	-0.01	0.00	0.23	-15	0.2
SPIT	0.00	0.01	0.18	-3	0.1
SPIT	0.00	0.01	0.24	-2	0.1
SPIT	-0.01	0.00	0.19	-12	0.2
SPIT	-0.07	-0.13	-0.59	-7	0.4
SPIT	0.01	0.03	0.40	-8	0.2
SPIT	-0.05	-0.08	-0.47	-11	0.2
SPIT	0.00	0.02	-0.61	-6	-1.0
SPIT	-0.06	-0.09	-0.61	-16	0.1
SPIT	-0.07	-0.08	-0.62	-25	0.1
SPIT	-0.01	-0.01	-0.45	-9	-0.3
SPIT	-0.06	-0.10	-0.66	-8	0.2
SPIT	0.08	0.15	0.45	-2	-0.8
SPIT	0.04	0.08	-1.07	3	-1.7
SPIT	-0.03	-0.05	-1.02	-5	-0.6
SPIT	-0.01	-0.01	-0.30	-4	-0.2
<b>1<math>\sigma</math></b>	<b>0.04</b>	<b>0.08</b>	<b>0.57</b>	<b>7</b>	<b>0.7</b>

845





848 Table S3 Continued:

Sample	$\delta^{17}\text{O}$	(1 $\sigma$ )	$\delta^{18}\text{O}$	(1 $\sigma$ )	$\delta\text{D}$	(1 $\sigma$ )	d-excess	$^{17}\text{O}$ -excess	Latitude (N)	Longitude (W)
<b>San Jose Lake</b>										
SJ 4-III-04 0m	-0.41	0.02	-0.75	0.02	-8.06	0.18	-2.1	-10	20° 52.316'	90° 8.252'
SJ 4-III-04 1m	-0.45	0.02	-0.86	0.03	-8.94	0.07	-2.0	4	20° 52.316'	90° 8.252'
SJ 4-III-04 2m	-0.16	0.02	-0.33	0.03	-4.60	0.13	-1.9	17	20° 52.316'	90° 8.252'
SJ 4-III-04 3m	-0.31	0.03	-0.63	0.03	-6.91	0.16	-1.9	19	20° 52.316'	90° 8.252'
SJ 4-III-04 4m	-0.37	0.03	-0.72	0.04	-7.08	0.14	-1.3	15	20° 52.316'	90° 8.252'
SJ 4-III-04 5m	-0.28	0.02	-0.55	0.02	-5.71	0.22	-1.3	10	20° 52.316'	90° 8.252'
SJ 4-III-04 6m	-0.25	0.02	-0.50	0.03	-5.41	0.08	-1.4	10	20° 52.316'	90° 8.252'
SJ 04-II-04 7 m	-0.35	0.01	-0.65	0.03	-6.31	0.17	-1.1	-5	20° 52.316'	90° 8.252'
SJ 4-III-04 8m	-0.23	0.02	-0.46	0.02	-5.07	0.07	-1.4	8	20° 52.316'	90° 8.252'
SJ 4-III-04 9m	-0.18	0.02	-0.37	0.02	-4.73	0.08	-1.8	11	20° 52.316'	90° 8.252'
SJ 4-III-04 10m	-0.29	0.03	-0.58	0.03	-6.57	0.14	-2.0	15	20° 52.316'	90° 8.252'
San Jose B surface #5	0.09	0.03	0.17	0.03	-3.87	0.09	-5.3	1	20° 52.316'	90° 8.252'
<b>Punta Laguna</b>										
Punta Laguna 3-IV-05	1.32	0.03	2.58	0.04	11.42	0.09	-9.4	-41	20° 38.888'	87° 38.128'
Punta Laguna 26-V-00 mid basin	0.76	0.02	1.45	0.03	5.83	0.17	-5.8	-6	20° 38.888'	87° 38.128'
Punta Laguna 26-V-00 east basin	1.05	0.03	2.00	0.05	8.40	0.17	-7.6	-8	20° 38.888'	87° 38.128'
Punta Laguna 3-VI-95	0.88	0.03	1.69	0.03	5.64	0.28	-8.9	-12	20° 38.888'	87° 38.128'
Punta Laguna 20-I-96 end of the dock	0.20	0.03	0.41	0.04	0.40	0.16	-3.9	-16	20° 38.888'	87° 38.128'
Punta Laguna 2-5-96	0.22	0.02	0.45	0.05	0.05	0.33	-4.5	-18	20° 38.888'	87° 38.128'
<b>Other lakes</b>										
Sacnab surf water 13-VIII-03	2.16	0.05	4.11	0.06	22.07	0.12	-10.8	-8	17° 03.0'	89° 22.0'
Sacnab west end 31-VIII-99	1.39	0.03	2.68	0.03	12.04	0.13	-9.3	-22	17° 03.0'	89° 22.0'
Lake Petenxil surface 16-VIII-03	2.12	0.02	4.05	0.02	15.03	0.17	-17.4	-16	17° 01.70'	89° 47.956'
Sayaucil # 2 deep	2.28	0.02	4.38	0.03	16.29	0.17	-18.8	-26	20° 41.037'	88° 48.73'
Sayaucil surface A #6	2.70	0.02	5.18	0.04	19.79	0.19	-21.6	-28	20° 41.037'	88° 48.73'
Sayaucil #2 deep	2.35	0.03	4.54	0.04	17.14	0.31	-19.2	-47	20° 41.037'	88° 48.73'
Sayaucil #6 surface	2.65	0.02	5.11	0.05	19.73	0.15	-21.1	-41	20° 41.037'	88° 48.73'
Yalahau #5	1.66	0.03	3.21	0.03	14.30	0.16	-11.3	-29	20° 39.4'	89° 13.1'
Lake Saepuy Surface	1.46	0.02	2.84	0.03	9.68	0.28	-13.0	-39	16° 59.4'	90° 3.1'
Lake Saepuy Surface 16-VIII-03	2.43	0.02	4.69	0.02	22.07	0.38	-15.5	-39	16° 59.4'	90° 3.1'
Lake Yaxha 13-8-03 4.2 m	1.72	0.04	3.29	0.04	16.31	0.21	-10.0	-12	17° 3.5'	89° 24.5'
Tikal Aguada 13-VIII-01	2.68	0.02	5.14	0.03	19.46	0.15	-21.6	-30	17° 13.741'	89° 36.131'
Lake Quexil 16-VIII-03 surface	2.16	0.02	4.16	0.03	17.95	0.14	-15.3	-32	16° 55.5'	89° 48.1'
Uaxactun Aguada 13-VIII-01	0.57	0.03	1.10	0.04	-1.43	0.13	-10.2	-12	17° 23.643'	89° 38.077'
Santa Ana Vieja Aguada 14-VIII-01	-0.36	0.02	-0.66	0.04	-4.87	0.21	0.4	-8	16° 38.6'	89° 45.0'
Aguada Zapceten 30-I-2006	2.64	0.03	5.08	0.03	21.87	0.40	-18.8	-36	16° 59.255'	89° 39.602'
Laguna Milagros 15-V-02	1.23	0.03	2.34	0.04	11.42	0.34	-7.3	-6	18° 30.2'	88° 25.5'
Sayil little basin 4-III-05	1.92	0.02	3.69	0.04	14.29	0.21	-15.2	-21	20° 10.684'	89° 39.128'
Laguna near Xcaamal A 31-III-05	1.39	0.03	2.67	0.04	15.17	0.34	-6.5	-20	20° 36.599'	89° 42.907'
Laguna near Xcaamal B 31-III-05	1.40	0.03	2.71	0.04	15.66	0.16	-13.8	-35	20° 36.599'	89° 42.907'
Cenote 05-III-04 261B 0m	2.42	0.01	4.65	0.02	18.69	0.16	-18.5	-29	20° 35.707'	89° 42.70'
Cenote 261 A Surf	3.01	0.02	5.82	0.05	23.21	0.32	-23.3	-57	20° 35.707'	89° 42.70'
Cenote 261 95B 2-VIII-2005	1.69	0.02	3.26	0.02	9.98	0.17	-16.1	-27	20° 35.707'	89° 42.70'
Cenote 261 B 26-II-05	2.59	0.01	4.98	0.03	20.23	0.23	-19.6	-37	20° 35.707'	89° 42.70'
Cenote 261 26-II-05	2.35	0.04	4.55	0.05	18.19	0.11	-18.3	-48	20° 35.707'	89° 42.70'
Cenote 261 21-VIII-05	1.23	0.02	2.43	0.03	4.78	0.06	-14.6	-47	20° 35.707'	89° 42.70'
Quexil shore 7-III-2005	2.03	0.05	3.93	0.07	17.57	0.49	-13.8	-36	20° 35.707'	89° 42.70'
Cenote X'caamal #96B 2-VIII-2005	0.63	0.02	1.22	0.03	-0.55	0.09	-10.3	-13	20° 35.707'	89° 42.70'
Monifata 7-VIII-97	0.79	0.02	1.52	0.05	2.66	0.25	-9.5	-10	16° 55.343'	89° 50.247'
La Gloria 21-VIII-09	0.87	0.02	1.72	0.05	3.80	0.33	-10.0	-36	16° 56.745'	90° 22.495'
Uxmal Fountain	0.10	0.03	0.20	0.03	-1.45	0.18	-3.0	-3	20° 21.672'	89° 46.091'
Yalahau surface #3 B	1.62	0.05	3.10	0.06	12.74	0.52	-12.1	-20	20° 39.447'	89° 12.979'
Yalahau deep #1 A	1.62	0.04	3.13	0.04	13.22	0.28	-11.8	-37	20° 39.447'	89° 12.979'
Well Macanche 28-VIII-99	1.46	0.02	2.80	0.03	13.31	0.25	-9.1	-23	16° 58.0'	89° 38.5'
Macanche surface 28-VIII-99	1.62	0.04	3.12	0.06	14.28	0.45	-10.7	-30	16° 58.0'	89° 38.5'
Amatitlan 13-III-2000 1m	-2.57	0.03	-4.91	0.03	-39.95	0.12	-0.7	28	14° 28.908'	90° 36.103'
Amatitlan 14-III-2000 core site	-1.63	0.03	-3.09	0.05	-29.25	0.26	-4.5	4	14° 28.908'	90° 36.103'
Amatitlan 15-III-2000 core site	-2.77	0.04	-5.28	0.09	-42.11	0.51	0.1	23	14° 28.908'	90° 36.103'
Amatitlan 14-III-2000 hot spring	-2.98	0.05	-5.66	0.08	-48.06	0.65	-3.1	14	14° 28.908'	90° 36.103'
Coba deep #5	1.31	0.03	2.51	0.04	11.41	0.23	-8.6	-14	20° 29.652'	87° 44.308'
Coba deep #2	1.27	0.01	2.43	0.02	11.22	0.17	-8.3	-11	20° 29.652'	87° 44.308'
Coba surface #1A	1.30	0.03	2.47	0.04	10.86	0.16	-8.9	-8	20° 29.652'	87° 44.308'
Coba surface #1	1.26	0.01	2.41	0.02	10.81	0.15	-8.5	-9	20° 29.652'	87° 44.308'
Lake Coba 2-V-96	-0.15	0.02	-0.25	0.04	-3.69	0.17	-2.6	-16	20° 29.652'	87° 44.308'
L. Coba 2-VI-96	0.54	0.02	1.03	0.02	2.75	0.14	-5.5	0	20° 29.652'	87° 44.308'



852 **Table S5:**

853 Stable isotope ratios of rainwater from the Yucatán Peninsula.

854

Sample	$\delta^{17}\text{O}$	(1 $\sigma$ )	$\delta^{18}\text{O}$	(1 $\sigma$ )	$\delta\text{D}$	(1 $\sigma$ )	d-excess	$^{17}\text{O}$ -excess	Latitude (N)	Longitude (W)
RAIN Chichancanab 7-3-94	-1.44	0.04	-2.74	0.04	-14.22	0.54	7.7	14	19° 52.771'	88° 46.026'
RAIN Chichancanab 7-3-94 B	-1.20	0.25	-2.29	0.47	-13.38	1.52	7.3	11	19° 52.771'	88° 46.026'
RAIN-9-I-2007 3:30 PM	-0.09	0.02	-0.18	0.05	13.73	0.17	15.2	6	20° 0.993'	89° 1.218'
RAIN-30-III 3:00 PM	-1.50	0.03	-2.84	0.04	-18.16	0.36	4.6	-1	20° 0.993'	89° 1.218'
RAIN-25-I-2007 7:00 PM	0.26	0.05	0.47	0.07	15.40	0.41	11.6	6	20° 0.993'	89° 1.218'
RAIN 23-II-2007 8:00 PM	-0.08	0.04	-0.15	0.06	8.66	0.26	9.9	3	20° 0.993'	89° 1.218'
RAIN 8-III-2007 8:00	-0.96	0.02	-1.84	0.01	6.51	0.10	21.2	14	20° 0.993'	89° 1.218'
RAIN 15-I-2007 9:00	0.11	0.02	0.20	0.02	13.77	0.21	12.1	2	20° 0.993'	89° 1.218'
RAIN 5-VIII-2007 8:00	-2.80	0.02	-5.33	0.04	-30.52	0.29	12.2	16	20° 0.993'	89° 1.218'
RAIN 23-VI-2007 2:40PM	-1.29	0.03	-2.45	0.02	-14.16	0.25	5.5	1	20° 0.993'	89° 1.218'
RAIN 11-V-2007 9:30 PM	0.23	0.03	0.45	0.02	12.61	0.26	9.0	-4	20° 0.993'	89° 1.218'
RAIN 08-II-2017 1:00PM	-0.02	0.02	-0.05	0.04	11.26	0.37	11.7	3	20° 0.993'	89° 1.218'
RAIN 13-I-2007 2:15AM	0.43	0.02	0.80	0.03	16.43	0.32	10.0	5	20° 0.993'	89° 1.218'
RAIN 11-V-2007 9:30 PM	0.22	0.02	0.36	0.03	11.02	0.78	8.1	8	20° 0.993'	89° 1.218'
RAIN 08-II-2017 1:00PM	-0.03	0.02	-0.11	0.04	10.50	0.28	11.4	11	20° 0.993'	89° 1.218'
RAIN 13-I-2007 2:15AM	0.46	0.03	0.83	0.06	16.37	0.28	9.7	10	20° 0.993'	89° 1.218'
RAIN 06-II-2007 6:00PM	-0.42	0.05	-0.84	0.08	9.55	0.45	16.3	16	20° 0.993'	89° 1.218'
RAIN 12-I-2007 2:30PM	0.10	0.05	0.13	0.07	14.37	0.36	13.4	13	20° 0.993'	89° 1.218'
RAIN 6-II-2007 6:00 pm	-0.38	0.02	-0.78	0.03	10.11	0.12	16.3	29	20° 0.993'	89° 1.218'
RAIN 11-II-2007 5:00 PM	-1.09	0.02	-2.10	0.02	0.79	0.09	17.6	22	20° 0.993'	89° 1.218'
RAIN 12-I-2017 2:30PM	0.08	0.02	0.12	0.04	14.23	0.12	13.26	18	20° 0.993'	89° 1.218'
RAIN 29-IV-2007	0.10	0.02	0.18	0.02	15.12	0.29	13.70	4	20° 0.993'	89° 1.218'
RAIN 31-V-2017 6:00	-3.90	0.05	-7.37	0.07	-46.60	0.61	12.38	-2	20° 0.993'	89° 1.218'
RAIN 31-VII-2005	-0.60	0.03	-1.13	0.03	4.94	0.18	13.8	-1	20° 0.993'	89° 1.218'
RAIN Roof drain 31-VII- 2005	-0.60	0.03	-1.16	0.03	4.33	0.31	13.3	16	20° 0.993'	89° 1.218'
RAIN Punta Laguna 2-VI-96	0.23	0.05	0.42	0.06	11.63	0.16	8.2	7	20° 38.888'	87° 38.128'
RAIN Calcehtok 25-II-05	-0.48	0.03	-0.92	0.03	3.04	0.05	9.9	5	20° 33.041'	89° 54.740'
RAIN Peten Itza 21-I-96	-0.74	0.03	-1.41	0.03	1.50	0.16	12.8	4	17° 0.170'	89° 47.956'
RAIN Merida 16-VI-94	-0.63	0.03	-1.16	0.05	-3.03	0.08	6.2	-17	20° 58.654'	89° 37.407'
RAIN X'Caamal 8-VIII-01	0.20	0.02	0.39	0.03	4.97	0.20	1.8	-4	20° 36.599'	89° 42.907'
RAIN Piste 9-VI-96	-3.24	0.02	-6.15	0.03	-39.02	0.50	10.2	10	20° 41.53	88° 35.22

855 **Table S6:**  
856 Transient model parameters. See text for details of parameters.  
857

Category	Parameter	Units	Value
Lake Evaporation	Lake Temperature	°C	25
	w	-	0.5
	V <sub>eq</sub>	-	0.6
	Vapor Temperature	°C	25
	θ <sub>eq</sub>	-	0.529
	θ <sub>kin</sub>	-	0.518
Precipitation	δ <sup>18</sup> O	(per mil, VSMOW)	-4.5
	d-excess		10
	<sup>17</sup> O-excess		2.5
Groundwater	δ <sup>18</sup> O	(per mil, VSMOW)	-4.5
	d-excess		10
	<sup>17</sup> O-excess		2.5
	Ca	g/kg	0.607
	SO <sub>4</sub>		2.455
	Na		0.2
	Mg		0.2
	K		0.011
Cl	0.234		
Fluxes	F <sub>p</sub>	m water equivalent/m <sup>2</sup> /a	Reanalysis data = ~1
	F <sub>e</sub>		1.07
	F <sub>gb</sub>	kg (~m water equivalent/m <sup>2</sup> /a)	1.02e9 (~0.1)
	F <sub>bg</sub>		1.02e9 (~0.1)
	F <sub>b1b2</sub>		1.02e10 (~1.0)
	F <sub>b2b1</sub>		1.02e10 (~1.0)

858

859 **Table S7:**

860 Paleo-lake temperature calculations. The equation of Grossman and Ku (45) was used  
 861 to calculate the temperature at which the aragonitic shells of *Pyrgophorus coronatus*  
 862 formed.

863

Sample	$\delta^{18}\text{O}$ (Carbonate)	$\delta^{18}\text{O}$ (GHW)	Temperature (°C)
CHI 07-III-04 139.5-140.0 cm	3.40	4.07	24.9
CHI 07-III-04 133.0-133.5 cm	2.96	3.65	25.0
CHI 07-III-04 133.5-134.0 cm	3.46	3.87	23.7
CHI 07-III-04 140.5-141.0 cm	3.23	3.99	25.3
CHI 07-III-04 153.0-153.5 cm	3.06	4.07	26.4
CHI 07-III-04 154.0-154.5 cm	3.26	4.70	28.4
CHI 07-III-04 166.0-166.5 cm	2.59	3.85	27.6
<b>Mean</b>			<b>25.9</b>
<b>1<math>\sigma</math></b>			<b>1.7</b>

864 **Table S8:**

865 Steady-state parameters for Monte Carlo simulations. See text for details of

866 parameters.

867

Category	Parameter	Units	Values [Range]
Lake Evaporation	Lake Temperature	°C	[22 28]
	w	-	[0.5 0.6]
	V <sub>eq</sub>	-	[0.6 0.7]
	X <sub>e</sub>	-	[0.8 0.9]
	Vapour Temperature	°C	25
	θ <sub>eq</sub>	-	0.529
	θ <sub>kin</sub>	-	0.518
Precipitation	δ <sup>18</sup> O	(per mil, VSMOW)	[-5 -4]
	d-excess		[5 15]
	<sup>17</sup> O <sub>excess</sub>		[-7 12]

868



872 **Table S10:**

873 Output table of Bayesian age-depth analysis. Mean ages display single ‘best’ model  
 874 based on the weighted mean age for each depth. Positive and negative age errors  
 875 represent 95% confidence intervals.

Depth (cm)	Mean Age (C.E.)	Positive Age Error (C.E.)	Negative Age Error (C.E.)
0	2004.4	2025.6	1953.5
1	2000.8	2021.3	1948.7
2	1993.6	2019.6	1938.9
3	1986.5	2018.6	1920.1
4	1979.7	2018.5	1897.6
5	1972.9	2018.7	1874.6
6	1965.4	2014.2	1867.4
7	1958	2011.8	1859.3
8	1950.5	2010	1846.3
9	1943	2008.4	1831.4
10	1935.6	2006.6	1814
11	1928.4	2001.4	1805.9
12	1921	1997.7	1796.8
13	1913.7	1995.4	1787.2
14	1906.5	1993.2	1773.1
15	1899.2	1991.6	1758.2
16	1891.9	1985.5	1751.1
17	1884.4	1981.2	1744
18	1877.2	1978	1731.8
19	1869.9	1975.3	1719
20	1862.8	1973.4	1705
21	1855.6	1967.1	1698.7
22	1848.4	1961.7	1692.4
23	1841.2	1957.2	1684.3
24	1833.9	1953.8	1673.3
25	1826.7	1950.8	1661.2
26	1819.5	1942.6	1654.2
27	1812.4	1937.1	1648.5
28	1805.3	1932.8	1640.3
29	1798.2	1928.9	1630.3
30	1791.1	1925.5	1619.9
31	1783.7	1917.6	1612.2
32	1776.4	1911.4	1605
33	1769.1	1907.3	1597.2
34	1761.7	1902.1	1588.6
35	1754.3	1899.1	1576.3
36	1747.2	1889.9	1569.6
37	1740	1884.8	1562.5
38	1732.8	1878.6	1555.9
39	1725.6	1874.2	1546.3
40	1718.4	1870.9	1535.3
41	1711.1	1863.1	1530
42	1703.8	1856.5	1524.1
43	1696.5	1851	1515.5
44	1689.3	1846.6	1506.5
45	1682	1843	1499.4
46	1674.9	1836	1494.1
47	1667.6	1829.3	1488
48	1660.4	1824.2	1480.7
49	1653.1	1820	1471.6
50	1646	1817.4	1463.2
51	1638.8	1808.4	1457.4
52	1631.7	1801.1	1450.9
53	1624.5	1794.7	1443.7
54	1617.5	1788.8	1433.9
55	1610.6	1783.3	1424
56	1603.3	1774.4	1418.9
57	1596	1767.7	1411.9
58	1588.7	1761.3	1404.7
59	1581.3	1756.1	1395.4
60	1574.3	1752.8	1386.9
61	1567	1742.5	1382.3
62	1559.7	1735.3	1377.7
63	1552.4	1730	1370.6
64	1544.9	1722.8	1363.1
65	1537.5	1716.8	1353.5
66	1530.2	1706.5	1349.3
67	1522.8	1698.3	1344.9
68	1515.2	1692.2	1338.1
69	1507.7	1687.9	1331.8
70	1500.3	1683	1323.9
71	1493.2	1671.5	1319.3
72	1486.2	1664.5	1313.4
73	1479.2	1658	1305.6
74	1472	1653.6	1297.6
75	1465	1648.5	1290.1
76	1457.7	1638.8	1285.7
77	1450.5	1631.8	1280.5
78	1443.2	1625.4	1273.7
79	1435.9	1620.4	1267.4
80	1428.6	1614	1258.6
81	1421.8	1604.9	1253.8
82	1415.1	1595.6	1248.3
83	1408.2	1588.2	1241.6
84	1401.5	1581.9	1234.6
85	1394.6	1576.8	1225.3
86	1387.7	1567.5	1221.4
87	1380.6	1557.7	1216.6



876 Table S10 Continued:

Depth (cm)	Mean Age (C.E.)	Positive Age Error (C.E.)	Negative Age Error (C.E.)
88	1373.7	1549.7	1211.5
89	1366.7	1543	1204.8
90	1359.8	1537.7	1195.6
91	1352.9	1529.9	1191.4
92	1345.8	1522	1186.4
93	1338.8	1517.1	1180.5
94	1331.8	1510.2	1174.9
95	1324.8	1505	1167.6
96	1317.7	1494.9	1164
97	1310.6	1483.8	1159.3
98	1303.4	1476.3	1153.2
99	1296.2	1469.1	1146.4
100	1288.9	1464.9	1138.6
101	1281.8	1452.1	1135.1
102	1274.5	1440.8	1130.8
103	1267.4	1432.4	1124.8
104	1260.1	1426.3	1118.1
105	1252.9	1419.7	1110.5
106	1245.3	1407.6	1107.3
107	1237.8	1397.7	1103.1
108	1230.2	1389.7	1098.2
109	1222.7	1383.5	1092.9
110	1215.1	1376.9	1085.2
111	1208.3	1365.3	1082.2
112	1201.6	1354.9	1078.7
113	1194.9	1345.4	1074.8
114	1188.2	1337	1070.4
115	1181.5	1329.3	1064.3
116	1174.6	1318.1	1061.3
117	1167.8	1308.8	1058.7
118	1160.8	1300.9	1055.5
119	1154	1293.2	1050.4
120	1147	1288.3	1044
121	1140.1	1274.1	1042.7
122	1133.3	1262.6	1040.7
123	1126.3	1252.7	1038
124	1119.2	1244.4	1034.8
125	1112.2	1237.9	1029
126	1105.6	1224.3	1027.2
127	1098.6	1211.8	1025.1
128	1091.7	1203	1021.4
129	1084.8	1195.7	1016.6
130	1078.1	1190.9	1010.3
131	1068.7	1175.8	1005.6
132	1059.4	1165.4	997.3
133	1050.2	1157.9	985
134	1041	1151.4	967.4
135	1032.2	1146.8	948
136	1019.3	1127.1	940.2
137	1006.2	1110.5	925.7
138	992.9	1099.2	902.2
139	979.7	1092	874.6
140	966.9	1087	847.5
141	953.1	1056.6	838.5
142	939.1	1029.7	828.4
143	925	1011.1	814.5
144	911.1	997.8	795.5
145	897.2	989.4	770.4
146	881.1	965.8	761
147	865	954.1	749.2
148	848.9	946	733.4
149	832.9	940.7	710.8
150	817	936.9	681
151	801	915.2	676.2
152	784.7	901.2	670.8
153	768.4	891.6	663.9
154	752.2	882.9	654.6
155	736.1	876.9	636.7
156	720.2	835.6	635.2
157	704.1	800.2	632.2
158	687.7	772.6	628.7
159	671.2	753.8	622.7
160	654.8	741.2	610
161	647	729.3	605.5
162	639.3	722.7	597.6
163	631.9	717.3	586.6
164	624.3	712.6	573.6
165	616.7	706.5	557.8
166	610.7	695.1	552.1
167	604.5	685.3	543.5
168	598.5	676.1	531.9
169	592.4	668.6	517.4
170	586.5	664.3	501
171	579.4	652.7	493.8
172	572.3	644.9	485.1
173	565.4	636.9	475.4
174	558.6	632.7	462.1
175	551.8	629.9	446.8

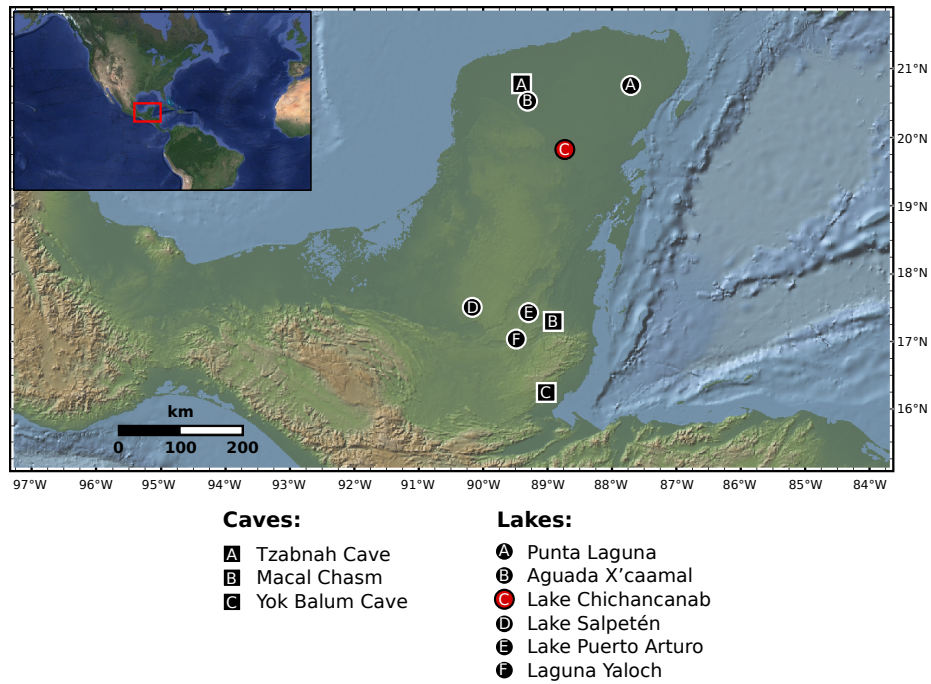
878 **Table S10 Continued:**

Depth (cm)	Mean Age (C.E.)	Positive Age Error (C.E.)	Negative Age Error (C.E.)
176	543.2	620.8	439.9
177	534.4	614.5	432.8
178	525.5	610	421.9
179	516.8	605.7	408.1
180	508.2	602.3	393.1
181	499.2	591.9	386.2
182	490.1	584	379.1
183	481.2	577.8	372
184	472.3	573.4	359.3
185	463.6	569.9	345.3
186	453	556.8	339.1
187	442.5	547.3	333.1
188	432	541.6	321.9
189	421.3	535.7	307.6
190	410.7	531.3	291.9
191	397.5	510.2	284.1
192	384.3	497.5	274.8
193	371.1	487.3	260.9
194	357.9	480.5	243.4
195	344.7	474.6	220.4
196	331.6	445.6	214.7
197	318.4	418.9	207.4
198	305.3	400.5	198.4
199	292.3	387.3	187.3
200	279.3	377.2	170.3
201	269.7	362.3	165.8
202	260	351.9	158.6
203	250.1	344	148.5
204	240.1	338.9	133.1
205	230.2	334.5	116.1
206	222	325.9	110.1
207	213.7	318.2	101.8
208	205.4	312.6	92.2
209	197.3	308.2	81.8
210	189.2	304.2	67.6
211	180.9	292.6	61.5
212	172.5	284.1	54.1
213	164.3	277.8	44.4
214	155.9	273.3	33.5
215	147.7	269.3	21.1
216	138.5	258.6	13.7
217	129.4	250.6	4.4
218	120.3	243.8	-8.6
219	111.1	239	-23.7
220	102.2	233	-42.4
221	92.1	223.8	-52.3
222	82.2	216.4	-67
223	72.5	210.5	-82.4
224	62.7	206	-101.8
225	52.9	202.7	-127.1
226	42.9	192.2	-136.3
227	32.8	185.8	-147
228	22.8	179.4	-160.1
229	12.7	174.2	-176
230	2.6	169.9	-196.4
231	-7.1	160.7	-207.1
232	-16.7	153.4	-217
233	-26.6	145.9	-228.7
234	-36.3	141	-243.2
235	-45.6	136.8	-264.2
236	-55.4	126.2	-271.6
237	-65.1	116.9	-281.5
238	-74.8	108.7	-292
239	-84.6	103	-306.6
240	-94.4	97	-322.6
241	-104.1	87.4	-328.6
242	-114	79.5	-336.7
243	-123.8	72.5	-347.8
244	-133.5	66.9	-362.9
245	-143.2	61.6	-378.6
246	-153.5	51	-388.6
247	-163.6	41.9	-396.6
248	-173.9	33.9	-407.9
249	-184.3	25.8	-420.7
250	-194.4	21.2	-436.8
251	-204.6	8.8	-446.1
252	-214.8	-1.1	-455.2
253	-224.9	-7.4	-465.3
254	-235	-13.6	-475.6
255	-244.9	-20.1	-491.8
256	-254.8	-30.3	-498.6
257	-264.7	-39.7	-507.6
258	-274.6	-47.6	-516.9
259	-284.8	-55.1	-528.2
260	-294.6	-62	-541.2

879

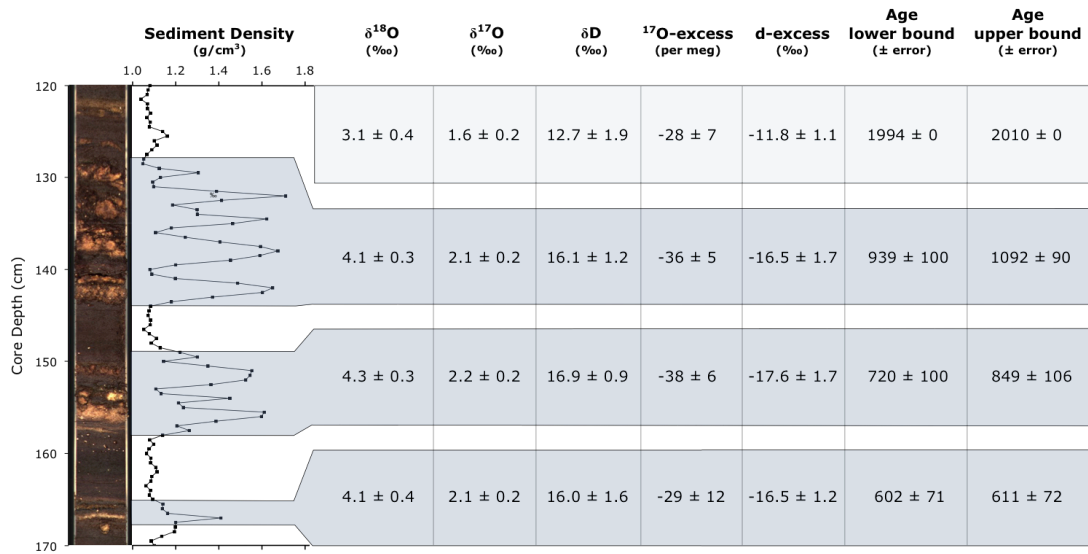
880 **Supplementary Figures:**

881



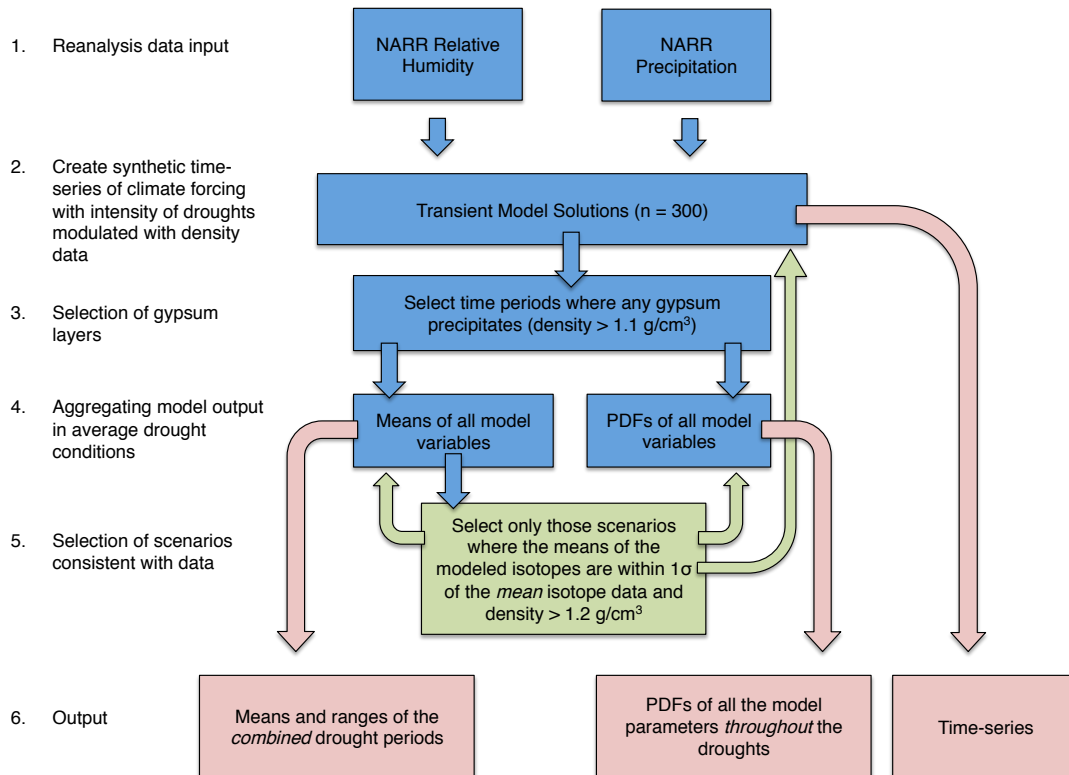
882

883 **Fig. S1:** Map of the Maya Lowlands displaying the locations of proxy climate  
884 archives (north to south); the Chaac speleothem of Tzabnah Cave (6); Punta Laguna  
885 (4); Aguada X'caamal (52); Lake Chichancanab (this study) (1-3); Lake Puerto Arturo  
886 (53); Laguna Yaloch (8); Macal Chasm (54); Lake Salpetén (9); the Yok I speleothem  
887 of Yok Balum Cave (7).



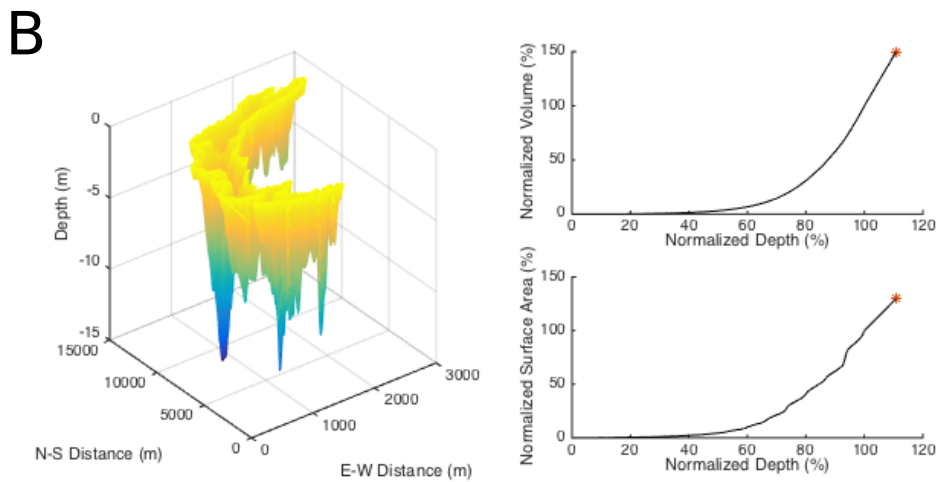
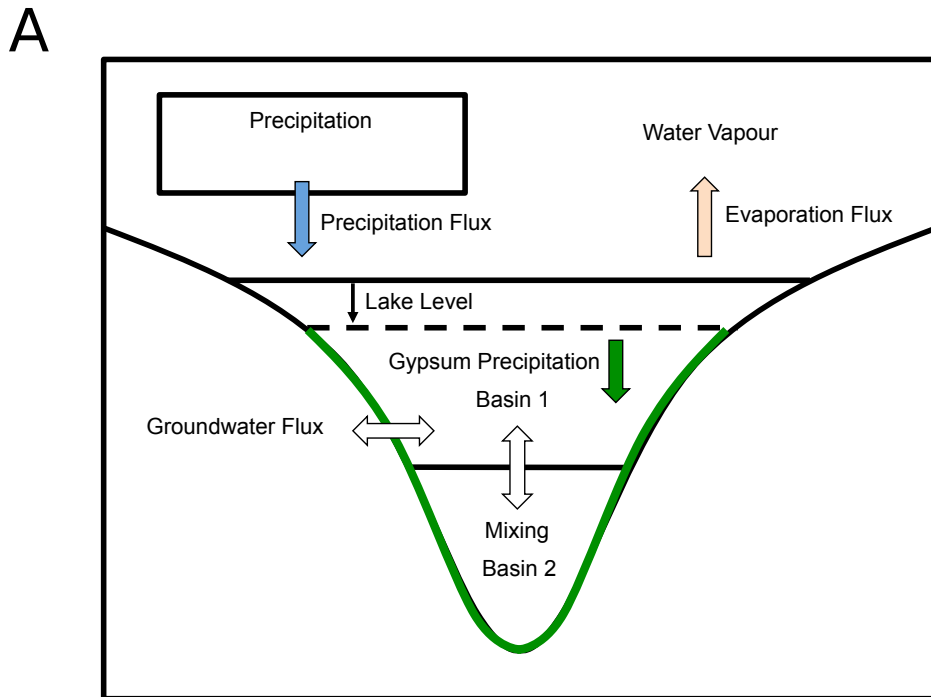
888

889 **Fig. S2:** (Left) Image of split core CH1 7-III-04 (3). Sediments are composed of  
 890 interbedded gypsum- and organic-rich strata containing abundant shell material. Solid  
 891 black line represents the GRA bulk density record measured on core CH1 7-III-04 (3).  
 892 Periods of gypsum precipitation are indicated by positive density excursions >1.2  
 893 g/cm<sup>3</sup>. (Right) The δ<sup>18</sup>O, δ<sup>17</sup>O, δD and d-excess (‰, VSMOW) and <sup>17</sup>O-excess (per  
 894 meg, VSMOW) (±1σ) of the modern lake water and measured GHW during each of  
 895 the three periods of gypsum deposition (after correction for known fractionation  
 896 factors (23) at 26°C) are displayed.



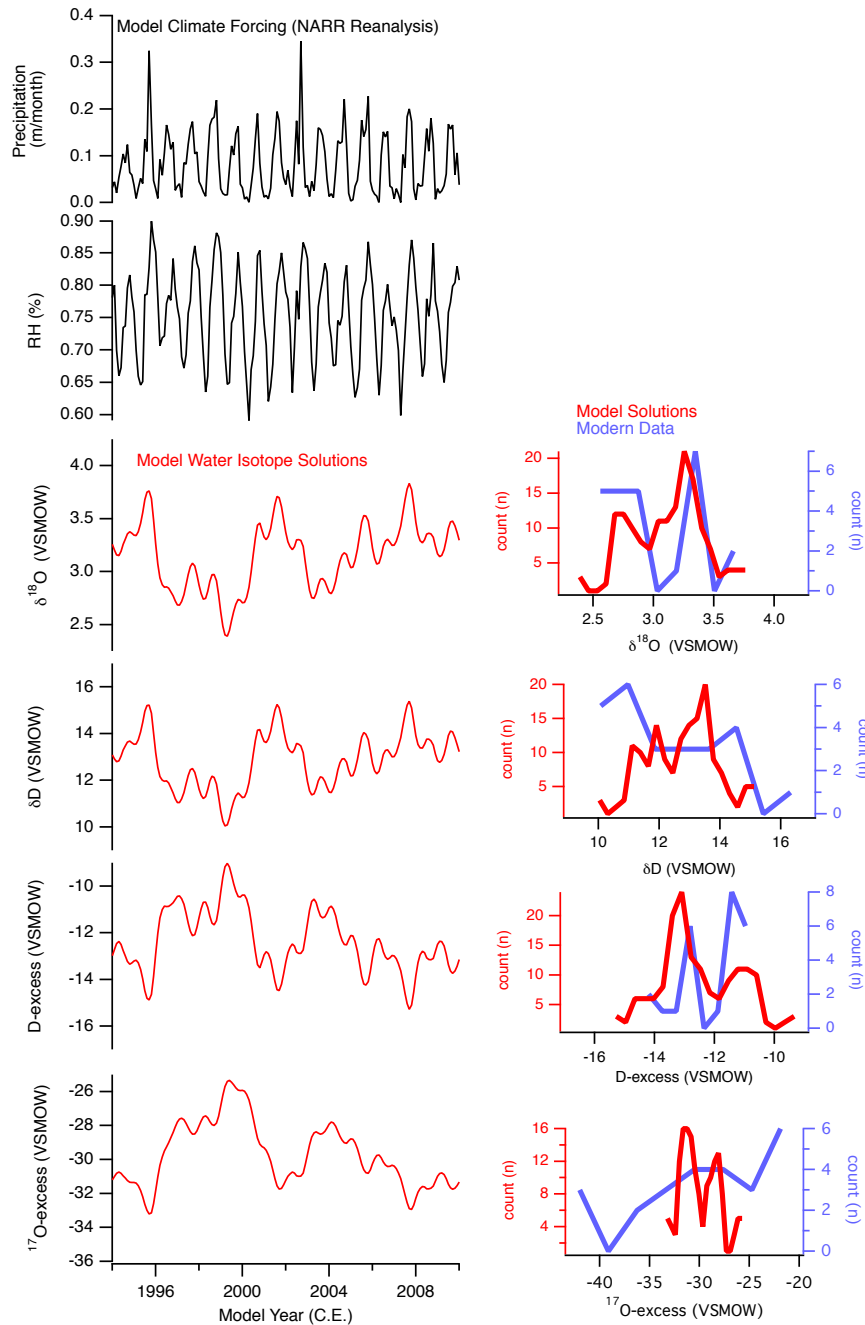
897

898 **Fig. S3:** Transient model summary of forcing (blue boxes and arrows), scenario  
 899 selection by model/data comparison (green boxes and arrows), and model output (red  
 900 boxes and arrows).



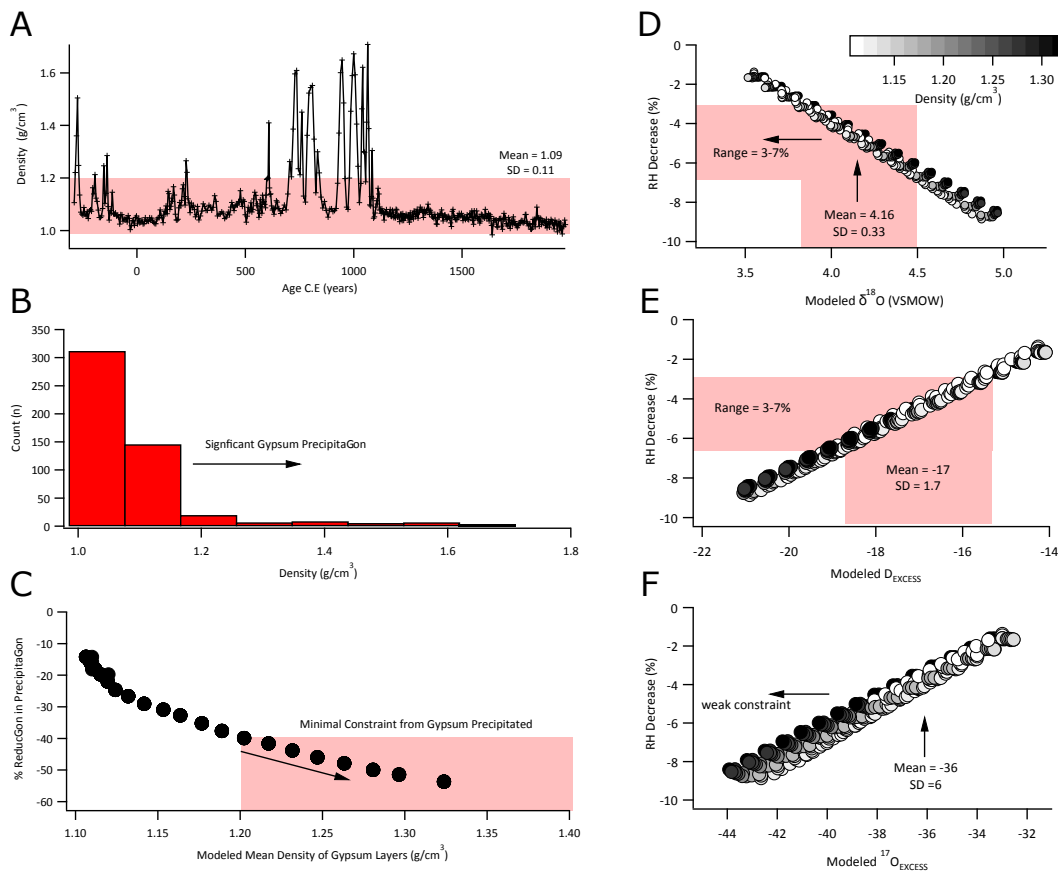
901

902 **Fig. S4:** (A) Diagrammatic representation of the two-box model used in transient  
 903 model scenarios. (B) The bathymetry of Lake Chichancanab used in the transient  
 904 model (3), and generated normalized surface area and volume vs normalized depth.



905

906 **Fig. S5:** Transient model climate forcing. The transient model is forced with North  
 907 American Regional Reanalysis (NARR) data for local precipitation and relative  
 908 humidity ( $\text{RH}_n$ ) across the modern sampling period from 1994 to 2010 (black lines).  
 909 Modeled water isotope solutions (red lines) are then compared to measured modern  
 910 data (blue lines) as histograms (right panel). The model successfully reproduced the  
 911 mean of modern isotope data, with insignificant gypsum precipitation. The time  
 912 interval from 1994 to 2010 is subsequently used as the baseline for comparison to  
 913 paleo-simulations.

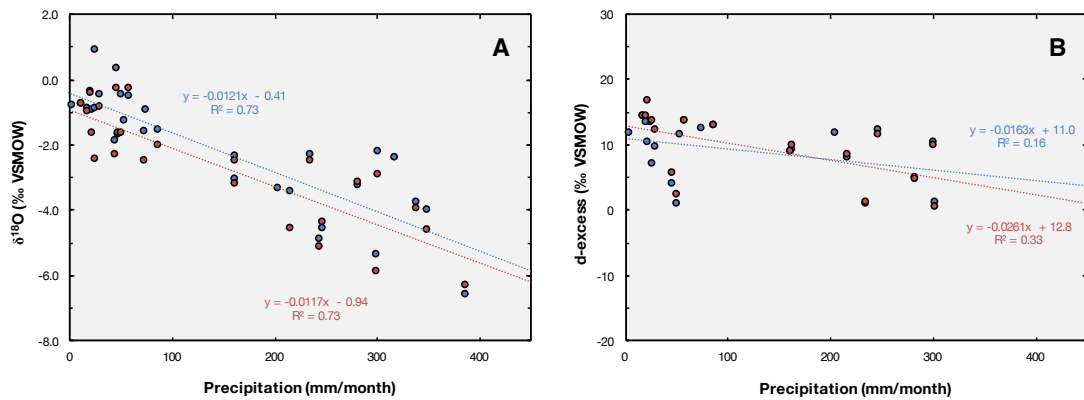


915

916

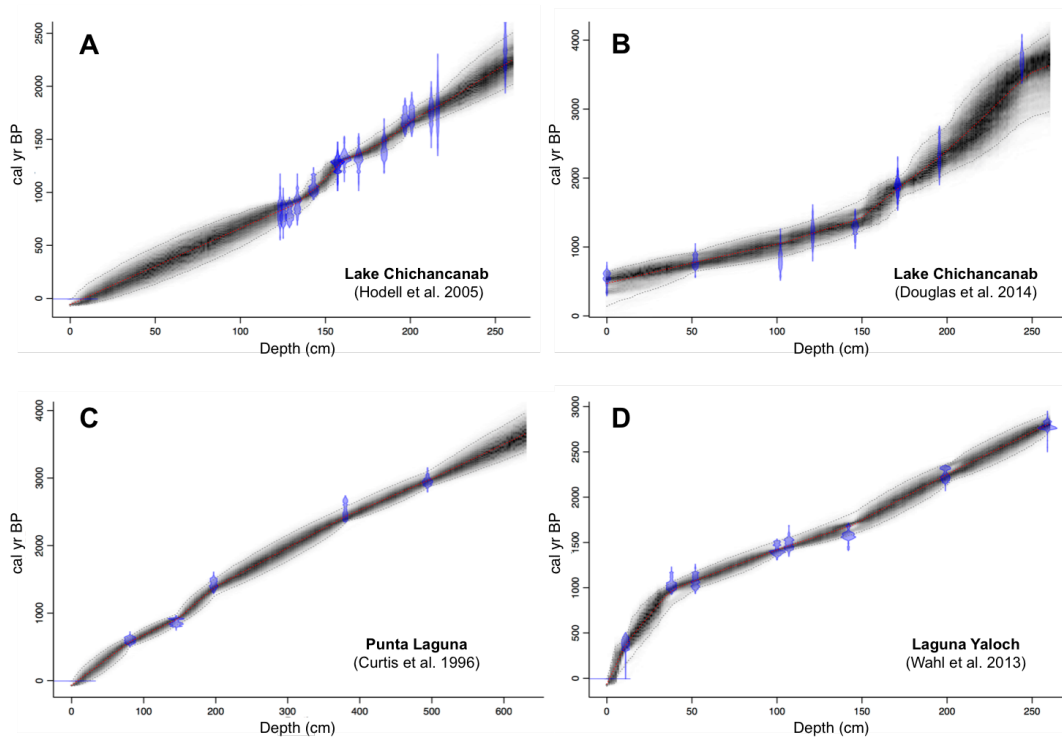
917 **Fig. S6:** Transient model precipitation and relative humidity scenarios. (A) GRA bulk  
 918 density record of core CH1 7-III-04 (3). From 500 B.C. to 2000 C.E., mean ( $\pm 1\sigma$ )  
 919 sediment density =  $1.09 \pm 0.11$  g/cm<sup>3</sup> (red horizontal band). (B) Histogram of counts  
 920 from GRA bulk density record from 500 B.C. to 2000 C.E. (C) Example of the  
 921 relationship between modeled mean core density (g/cm<sup>3</sup>) and the modeled reduction  
 922 in precipitation (%). Varying the minimum cut-off point from which modeled data are  
 923 compared to GHW data changes the baseline precipitation reduction estimate.  
 924 Example of modeled  $\delta^{18}\text{O}$  (D), d-excess (E), and  $^{17}\text{O}$ -excess (F) data plotted as a  
 925 function of modeled densities. Mean GHW ( $\pm 1\sigma$ ) data are then compared to modeled  
 926 runs to derive %RH<sub>n</sub> decrease.





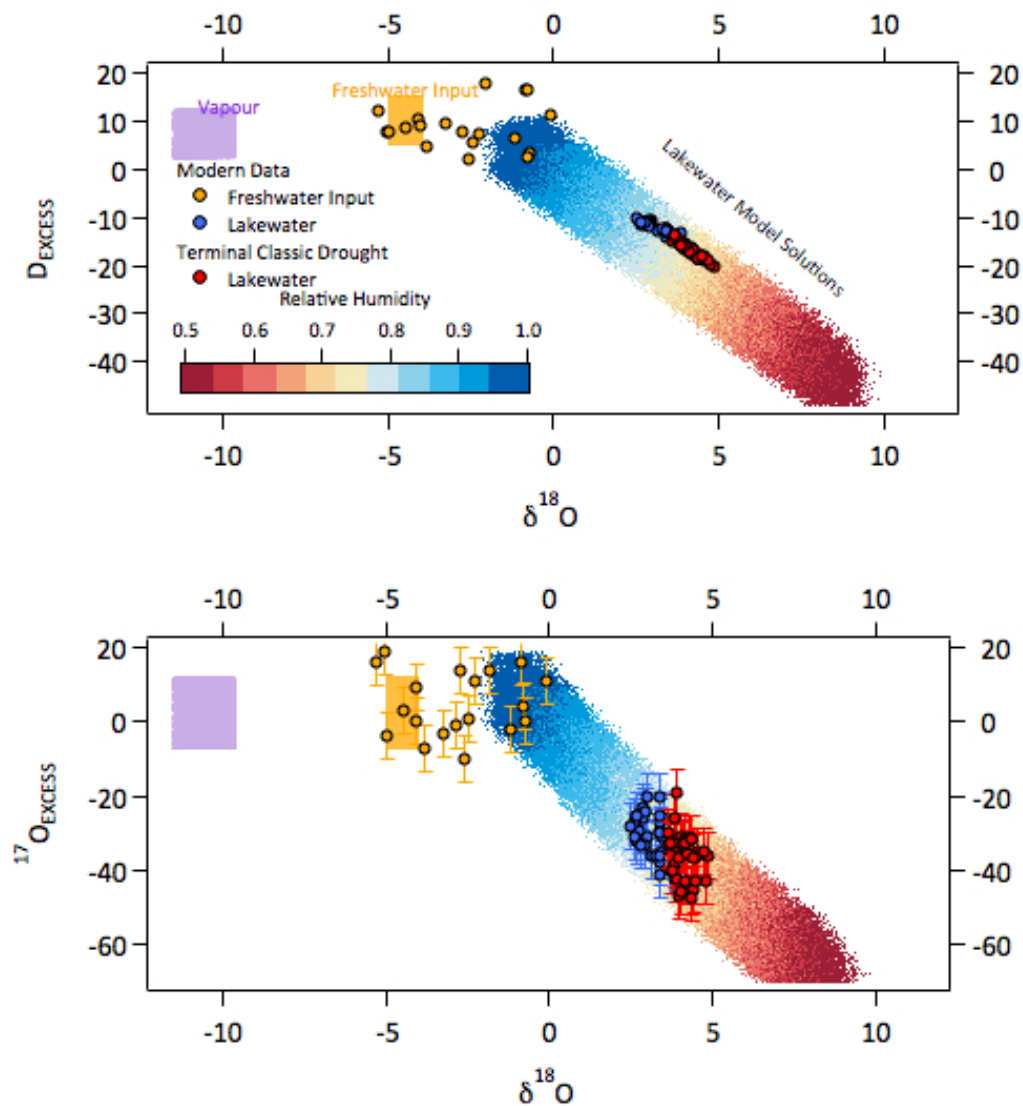
927

928 **Fig. S7:** The amount effect relationship between monthly precipitation amount and  
 929 monthly mean rainfall (A)  $\delta^{18}\text{O}$  and (B) d-excess during the dry (November to May)  
 930 and rainy seasons (June to October) from the IAEA station in Veracruz, México  
 931 (years 1969 to 1985) and Hobonil ( $20^{\circ}00'59''\text{N}$   $89^{\circ}01'13''\text{W}$ ; 2006 to 2009). Both raw  
 932 (blue circles) and amount-weighted (red circles) show that rainfall  $\delta^{18}\text{O}$  is negatively  
 933 correlated to the amount of precipitation on seasonal time scales, whereas there is no  
 934 significant amount effect displayed by d-excess.

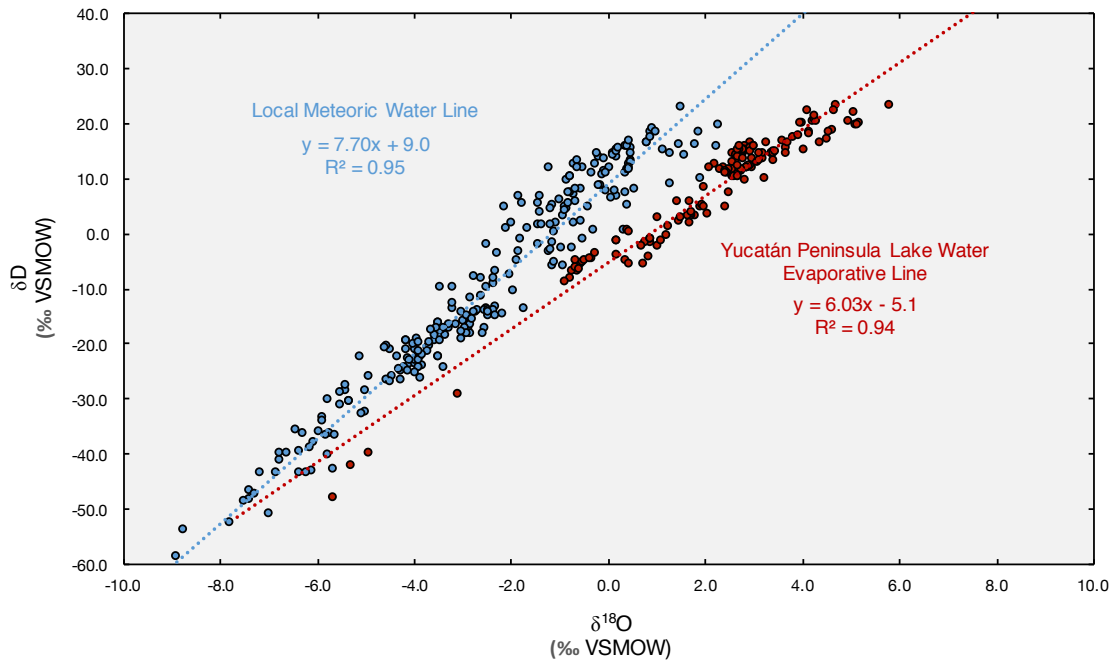


935

936 **Fig. S8:** Bayesian age models produced for (A) core CHI 7-III-04 of Lake  
 937 Chichancanab (3), (B) Plant waxes of Lake Chichancanab (50), (C) Punta Laguna (4)  
 938 and (D) Laguna Yaloch (8) by the program BACON (49). Dark shading indicates  
 939 more likely calendar ages at each depth and the red lines indicate the best-fit age  
 940 model.

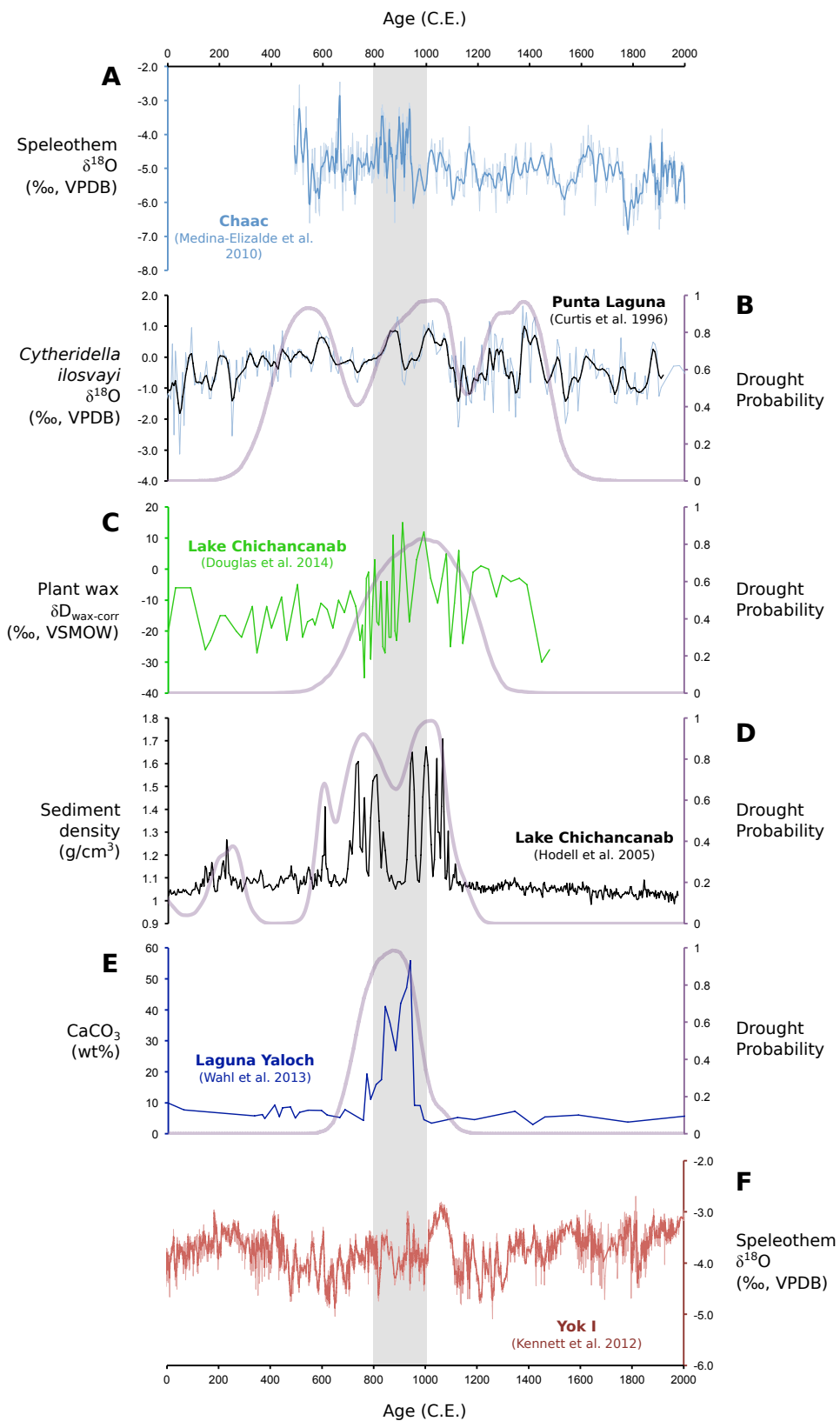


941  
 942 **Fig. S9:** Monte Carlo Modeling Scenarios in which the isotopic composition of the  
 943 paleo-lake water (red markers) and modern waters (blue markers) is shown in a cross  
 944 plot of  $\delta^{18}\text{O}$ -d-excess (upper panel) and  $\delta^{18}\text{O}$ - $^{17}\text{O}$ -excess (lower panel). Modern  
 945 freshwater data are shown (yellow markers). With the data, a suite of model solutions  
 946 are plotted with the assumed freshwater input range (yellow box), atmospheric water  
 947 vapor range (purple box) and the complete range of model solutions for the isotopic  
 948 composition of the lake with the marker coloring representing the range in normalized  
 949 relative humidity.



950

951 **Fig. S10:**  $\delta^{18}\text{O}$  and  $\delta\text{D}$  of rain, surface water, and ground water (blue circles). Dashed  
 952 blue line represents the local meteoric water line estimated by least-squares linear  
 953 regression through rain, surface and groundwater data. Red circles indicate  
 954 measurements made on lakes with varying hydrologic budgets and evaporative losses  
 955 across the Yucatán Peninsula. Dashed red line represents the evaporative line (with  
 956 slope = 6.0) estimated by least-squares linear regression using lake data. Note that this  
 957 slope is comparable to the slope of modern data from Lake Chichancanab alone (slope  
 958 = 5.1), and is significantly different from that of the slope of measured GHW data  
 959 (slope = 3.1) (Fig. 2).



960

961 **Fig. S11:** Selection of palaeoclimate records from the Maya Lowlands, arranged from  
 962 north to south: (A) Chaac speleothem (Tzabnah Cave)  $\delta^{18}\text{O}$  ( $\delta$ ); (B) Punta Laguna

963  $\delta^{18}\text{O}$  (4); (C) Lake Chichancanab  $\delta\text{D}_{\text{wax-corr}}$  (50); (D) Lake Chichancanab sediment  
964 density (3) (E) Laguna Yaloch weight percent calcium carbonate ( $\text{CaCO}_3$ ) (8); (F)  
965 Yok I speleothem (Yok Balum Cave)  $\delta^{18}\text{O}$  (7). Age uncertainty analysis for proxy  
966 sites displays “drought probabilities” in given time intervals for the proxy data. All  
967 age models were calculated using Bayesian age analyses (Fig. S8). The vertical gray  
968 bar indicates the TCP between 800 and 1000 C.E.  $\delta\text{D}_{\text{wax-corr}}$  values indicate  $\delta\text{D}_{\text{wax}}$   
969 values corrected for the influence of vegetation change (50). **Abbreviation:** VPDB,  
970 Vienna Pee Dee Belemnite; VSMOW, Vienna Standard Mean Ocean Water.

971 **Supplementary References:**

972

973 [31] E. Playa, C. Recio, J. Mitchell. Extraction of gypsum hydration water for oxygen  
974 isotopic analysis by the guanidine hydrochloride reaction method. *Chem. Geol.*  
975 **217**(1), 89-96 (2005).

976

977 [32] E. J. Steig, V. Gkinis, A. J. Schauer, S. W. Schoenemann, K. Samek, J.  
978 Hoffnagle, K. J. Dennis, S. M. Tan. Calibrated high-precision  $^{17}\text{O}$ -excess  
979 measurements using laser-current tuned cavity ring-down spectroscopy. *Atmos. Meas.*  
980 *Tech.* **7**, 2421–2435 (2014).

981

982 [33] S. W. Schoenemann, A. J. Schauer, E. J. Steig. Measurement of SLAP and GISP  
983  $\delta^{17}\text{O}$  and proposed VSMOW-SLAP normalization for  $^{17}\text{O}$ -excess. *Rapid Commun.*  
984 *Mass Spec.* **27**, 582–590 (2013).

985

986 [34] E. Barkan, B. Luz. Diffusivity fractionations of  $\text{H}_2^{16}\text{O}/\text{H}_2^{17}\text{O}$  and  $\text{H}_2^{16}\text{O}/\text{H}_2^{18}\text{O}$  in  
987 air and their implications for isotope hydrology. *Rapid Commun. Mass Spectrom.* **21**,  
988 2999–3005 (2007).

989

990 [35] A. L. Grauel, D. A. Hodell, S. F. Bernasconi. Quantitative estimates of tropical  
991 temperature change in lowland Central America during the last 42 ka. *Earth Planet.*  
992 *Sci. Lett.* **438**, 37–46 (2016).

993

994 [36] J. Li, M. Li, X. Fang, G. Zhang, W. Zhang, X. Liu. Isotopic composition of  
995 gypsum hydration water in deep Core SG-1, western Qaidam basin (NE Tibetan  
996 Plateau), implications for paleoclimatic evolution. *Glob. Planet. Change.* **155**, 70–77  
997 (2017).

998

999 [37] M. C. Ball, L. S. Norwood. Studies in the system calcium sulphate–water. Part I.  
1000 Kinetics of dehydration of calcium sulphate dihydrate. *Journal of the Chemical*  
1001 *Society A: Inorganic, Physical, Theoretical*, 1633-1637 (1969).

1002

- 1003 [38] J. K. Warren. *Evaporites: A geological compendium* (Springer, New York,  
1004 2016).  
1005
- 1006 [39] C. Spötl, T. W. Vennemann, Continuous-flow isotope ratio mass spectrometric  
1007 analysis of carbonate minerals. *Rapid Commun. Mass Spectrom.* **17**, 1004–1006  
1008 (2003).  
1009
- 1010 [40] E. Perry, G. Velazquez-Oliman, L. Marin. The hydrogeochemistry of the karst  
1011 aquifer system of the northern Yucatán Peninsula Mexico. *Int. Geol. Rev.* **44**, 191–  
1012 221 (2002).  
1013
- 1014 [41] R. E. Criss. *Principles of Stable Isotope Distribution* (Oxford Univ. Press,  
1015 Oxford, U.K. 1999).  
1016
- 1017 [42] J. Horita, D. J. Wesolowski. Liquid-vapor fractionation of oxygen and hydrogen  
1018 isotopes of water from the freezing to the critical temperature. *Geochim. Cosmochim.*  
1019 *Acta.* **58**, 3425–3437 (1994).  
1020
- 1021 [43] E. Barkan, B. Luz. High precision measurements of  $^{17}\text{O}/^{16}\text{O}$  and  $^{18}\text{O}/^{16}\text{O}$  ratios in  
1022  $\text{H}_2\text{O}$ . *Rapid Commun. Mass Spectrom.* **19**(24), 3737–3742 (2005).  
1023
- 1024 [44] J. J. Gibson, S. J. Birks, Y. Yi. Stable isotope mass balance of lakes: a  
1025 contemporary perspective. *Quat. Sci. Rev.* **131**, 316–328 (2016).  
1026
- 1027 [45] E. L. Grossman, T. Ku. Oxygen and carbon fractionation in biogenic aragonite:  
1028 temperature effect. *Chem. Geol.* **59**, 59–74 (1986).  
1029
- 1030 [46] R. Uemura, E. Barkan, O. Abe, B. Luz. Triple isotope composition of oxygen in  
1031 atmospheric water vapor. *Geo. res. let.* **37**(4) (2010).  
1032



- 1033 [47] R. Soler-Bientz, S. Watson, D. Infield. Wind characteristics on the Yucatán  
1034 Peninsula based on short term data from meteorological stations. *Energy Conversion*  
1035 *and Management*, **51**(4), 754-764 (2010).
- 1036
- 1037 [48] Z. Sofer, J. R. Gat. The isotope composition of evaporating brines: effect of the  
1038 isotopic activity ratio in saline solutions. *Earth Planet. Sci. Lett.* **26**, 179–186 (1975).
- 1039
- 1040 [49] M. Blaauw, J. A. Christen. Flexible paleoclimate age-depth models using an  
1041 autoregressive gamma process. *Bayesian Anal.* **6** (3), 457-474 (2011).
- 1042
- 1043 [50] P. M. Douglas, M. Pagani, T. I. Eglinton, M. Brenner, D. A. Hodell, J. H. Curtis,  
1044 K. F. Ma, A. Breckenridge. Pre-aged plant waxes in tropical lake sediments and their  
1045 influence on the chronology of molecular paleoclimate proxy records. *Geochim.*  
1046 *Cosmochim. Acta* **141**, 346–364 (2014).
- 1047
- 1048 [51] T. Bhattacharya, J. C. H. Chiang, W. Cheng. Ocean-atmosphere dynamics linked  
1049 to 800-1050 CE drying in Mesoamerica. *Quatern. Sci. Rev.* **169**, 263-277 (2017).
- 1050
- 1051 [52] D. A. Hodell, M. Brenner, J. H. Curtis, R. Medina-Gonzalez, E. I. Can, A.  
1052 Albornaz-Pat, T. P. Guilderson. Climate change on the Yucatán Peninsula during the  
1053 Little Ice Age. *Quat. Res.* **63**, 109–21 (2005).
- 1054
- 1055 [53] D. Wahl, R. Byrne, L. Anderson. An 8700 year paleoclimate reconstruction from  
1056 the southern Maya lowlands. *Quat. Sci. Rev.* **103**, 19–25 (2014).
- 1057
- 1058 [54] J. W. Webster, G. A. Brook, L. B. Railsback, H. Cheng, R. L. Edwards, C.  
1059 Alexander, P. P. Reeder. Stalagmite evidence from Belize indicating significant  
1060 droughts at the time of Preclassic Abandonment, the Maya Hiatus, and the Classic  
1061 Maya collapse. *Palaeogeogr. Palaeoclimatol. Palaeoecol.* **250**, 1–17 (2007).